November 2017

Design and Modeling of a High-Power Periodic Spiral Antenna with an Integrated Rejection Band Filter

Jonathan M. O'Brien
University of South Florida, jmo10@bellsouth.net

Design and Modeling of a High-Power Periodic Spiral Antenna

with an Integrated Rejection Band Filter

by

Jonathan M. O'Brien

A dissertation submitted in partial fulfillment
of the requirements for the degree of
Doctor of Philosophy
Department of Electrical Engineering
College of Engineering
University of South Florida

Co-Major Professor: Thomas M. Weller, Ph.D.
Co-Major Professor: Gokhan Mumcu, Ph.D.
Larry Dunleavy, Ph.D.
Stephen Saddow, Ph.D.
Nathan Crane, Ph.D.
Dorothy Poppe, Ph.D.

Date of Approval:
October 30, 2017

Keywords: Three Dimensional Miniaturization, Ultra-Wideband Antennas, Interference
Mitigation, Miniaturization Techniques, Notch Filter

DEDICATION

To my family

My mother who never let me quit at anything

My father who taught me that life isn't a destination

Joey who made me understand more about life than I could ever explain

My brother for being my best competitor in school

My best sister who can always make me laugh

Kelsey for being my life's adventure partner

ACKNOWLEDGMENTS

TABLE OF CONTENTS

LIST OF TABLES

LIST OF FIGURES

iv

v

ABSTRACT

This work details the design and fabrication of an ultra-wideband periodic spiral antenna (PSA) with a notch filter embedded directly into the radiating aperture. Prototype fabrication of the PSA reveals long assembly time due to forming the antenna element, therefore modifications are made to allow fabricating the antenna elements on a thin, flexible, Polyimide substrate. A transmission line model is develop to support the updated configuration of the antenna elements. In addition, a symmetric spurline filter is integrated into the arms of the spiral antenna in order to address the common problem of interference in ultra-wideband systems. For the first time, a placement study is conducted to show the optimal location of the filter as a function of frequency. The presented transmission line model demonstrates the ability to decouple the design of the filter and antenna by being able to predict the resonant frequency and achieved rejection after integration of the two. Measured results show a gain rejection of 21 dB along with the ability to tune the resonance of the filter from 1.1 – 2.7 GHz using a lumped capacitor. For high power applications, thermal measurements are conducted, and for the first time, thermal profiles along the top of the antenna are used to show the radiation bands in a spiral antenna. Power tests are successfully conducted up to 40 W across the entire operational bandwidth and up to 60 W for 2 GHz and below. At these elevated power levels, a large voltage is generated across the lumped capacitor used to tune the resonance of the spurline filter; this issue is addressed through the development of a capacitive wedge that is overlapped on top of the spurline stub, which increases the voltage handling to 2,756 V. Measured results reveal a reduced tuning range compared to using lumped capacitors and a gain rejection of greater than 10 dB for all configurations.

CHAPTER 1: INTRODUCTION

1.1. Motivation

The radio frequency (RF) spectrum that is occupied by terrestrial communication systems spans multiple octaves of bandwidth and utilizes numerous modulation schemes. The advent and progress of software defined radios improves the operational frequency range to encompass a large portion of this bandwidth, placing emphasis on an antenna structure equally as capable. When properly implemented these ultra-wideband (UWB) systems provide an all-in-one solution to today's frequency diverse communication systems.

While an UWB communication system can allow simultaneous reception of multiple standards the inability to attenuate potential high power interfering signals leaves the systems susceptible. If the unwanted signal is of known, fixed, frequency and bandwidth a notch filter can be added between the antenna and RF front end to reduce the incoming power to a safe level while adding loss, and therefore noise, to the link budget. Alternatively, implementing a tunable resonant antenna can help mitigate these interfering signals at the expense of system level capability. Resonant antennas have the advantage of being able to reject signals out of the band of interest, reducing the complexity and robustness of a filtering system. Including the capability to tune a resonant antenna allows the system to select the frequency band of interest, but literature has shown restrictions to tuning range as well as the system level consideration of only being able to receive a single frequency band at a time.

1

There is a desire for a system capable of handling multiple communication standards while being robust enough to attenuate an interfering signal of unknown frequency yet still maintaining a low size, weight, and power (SWAP).

1.2. Major Technical Challenges

During the development of this work the following technical challenges were addressed and presented in the following chapters.

a.) Miniaturization of an ultra-wideband antenna

b.) Mitigation against interfering signals

c.) High power handling capability

1.3. Technical Approach and Significance

An ultra-wideband antenna provides the ability to use a single antenna for multiple communication protocols. To be useful, the ultra-wideband antenna must have stable radiation characteristics to avoid the requirement for a frequency dependent physical configuration of the antenna. Historically, ultra-wideband antennas are significant in size due to their need to be appreciable in wavelength [3]. Developing a technique to efficiently miniaturize an ultra-wideband antenna, while simultaneously mitigating against interfering signals, opens the door for a greater number of uses that are size, weight, and power restricted.

While the uses of an ultra-wideband antenna are numerous, its benefit of radiating over multiple octaves of bandwidth can also come as a downfall. A common issue pertains to an undesired interfering signal either pushing the first stage low noise amplifier (LNA) into compression or increasing the noise floor of the receiver therefore decreasing the signal to noise

2

ratio (SNR). The ability to attenuate the interferer is typically addressed by introducing a filter block prior to the LNA. This filter block introduces additional loss in the receiver adding directly to the noise figure of the receiver.

A spiral antenna is known for its stable radiation pattern over multiple octaves of bandwidth. This stability extends itself to the axial ratio, beamwidth, gain, return loss, and efficiency therefore proving to be a good candidate for multipurpose radios. The miniaturization of spiral antennas has been studied extensively and lead to numerous techniques, each well documented in the literature.

A volumetric approach to miniaturization of a spiral antenna, the periodic spiral antenna, is developed in [4] which demonstrates a higher level of miniaturization than other planar techniques. Improving upon this work, a new fabrication technique is proposed which reduces assembly time from hours to minutes while increasing resolution in the z-direction to microns. Power handling capability of the cavity backed periodic spiral antenna is quantified with thermal measurements provided up to 60 watts of incident power. The introduction of a symmetric spurline notch filter into the radiating aperture of the periodic spiral antenna provides a technique to attenuate a known interfering signal without impacting the gain of the antenna outside of the rejection band or introducing additional loss prior to the first stage LNA. A transmission line model is developed and proven to allow the spurline filter to be developed separate from the antenna. A lumped capacitor is place at the end of the spurline filter allowing for tuning of the resonant frequency for low power applications. The development and integration of a conductive wedge placed on top of the spurline filter allows for modulation of the loading capacitance with an improved power handling capability.

3

1.4. Contributions

a.) Volumetrically optimized electrically small antennas

The results of developing volumetrically optimized antennas show an underlying general approach to improving performance of electrically small antennas. An innovative approach to the design of a loop antenna demonstrates significant improvements to miniaturization and efficiency. This technique provides a useful conceptual understanding that can be applied to the miniaturization of a spiral antenna.

b.) Fabrication process of the periodic spiral antenna

Arranging the spiral arms such that the width of the conductor lies orthogonal to the plane of the radiating aperture enables the conductor to be fabricated with flex circuit technology. Using a dry etch process to pattern the z-dimension of the periodic spiral antenna arms increases the resolution to microns. A groove to hold the flex circuit is designed in a 3D printed ULTEM 1000 substrate with a positional accuracy of +/- 89 µm according to statistical data provided by Fortus. These improvements reduce assembly time from hours to minutes.

c.) Development of an equivalent transmission line model for the non-radiating portion of the periodic spiral antenna

A new approach to model the miniaturization of a periodic spiral antenna is proposed using an equivalent transmission line model for the non-radiating portion of the periodic spiral antenna. This model demonstrates the ability to predict both the rejection and quality factor of a spurline filter prior to embedding it into a spiral antenna, therefore expediting the design cycle.

4

d.) Integrating notch filters in the radiating aperture of a spiral antenna

Numerous examples exist in the literature of resonant structures being added to ultra-wideband antennas to introduce a reduction in gain at a specific frequency. A majority of these implications exhibit around 10 dB of rejection with no known work presented that optimizes the location of these filters. A method for integrating a notch filter into the arms of a spiral antenna with improved rejection is presented here. Furthermore, the ability to decouple the filter design from the antenna design provides a method to reduce computational resources.

e.) Improve power handling of capacitive loaded spurline filter integrated into a spiral antenna

Developing a conductive wedge to be placed over the spurline filter allows tuning of the resonant frequency while increasing the power handling capability. The proposed design also maintains a low profile to minimize the impact to adjacent arms of the spiral antenna.

1.5. Dissertation Organization

Chapter two begins the discussion of this proposal by introducing some background information on antennas and their theory of operation. The chapter begins with a brief example of resonant antennas and the relationship between their current density and parameters such as radiation pattern and input impedance. The topic of antenna miniaturization is introduced by the discussion of two commonly used miniaturization techniques, dielectric loading and planar meandering. The theoretical limit of miniaturization is explained with Chu's theory which concentrates of relating spherical volume to quality factor. This chapter is concluded by investigating some of the recent advancements in interference mitigation techniques.

Chapter three introduces the design of the periodic spiral antenna. Improvements to the fabrication technique result in a new configuration for the conductors of the spiral arms where the width of the conductor lies orthogonal to the radiating aperture. This configuration lends itself to a system where the spiral arms are manufactured on a flexible substrate and placed down into the main antenna dielectric. Not only does the proposed manufacturing process reduce assembly time by a factor of 10, but it also improves the achieved miniaturization factor. The thermal impact of the proposed process is studied and thermal images are produces and related to the radiation bands in the spiral.

Chapter four shows the design and implementation of a spurline notch filter within the periodic spiral antenna. The development of an equivalent transmission line model allows for the filter and antenna to be designed independently reducing computational resources. A transmission matrix for the spurline filter is presented for both a static and tunable version. Proper placement of the filter is investigated through full wave simulation and related to basic operational theories for spiral antennas. Correlation between the calculated rejection and resonant frequency of the spurline filter and measured results from the embedded filter is presented.

Chapter five proposes an alternative design to capacitive loading the spurline filter while improving the power handling restriction imposed by the lumped capacitors. Full wave simulation results using the transmission line model with an incident power of 30 W show up to 227 V induced within the Parylene insulator while it is expected to withstand 2,756 V. Measured results demonstrate the ability to tune the rejection frequency of the integrated spurline filter with the proposed capacitive wedge.

6

CHAPTER 2: LITERATURE REVIEW

2.1. Antenna Operational Principles

Antennas are defined as transducers. They convert time dependent electrical currents into spherically propagating transverse electromagnetic waves. Typically, the oscillating current is introduced to the antenna at a specific location where a favorable impedance is presented to ensure maximum power transfer. Depending on geometry, antennas can be designed to radiate equally in all directions or focus the energy into a select area. Antennas which truly radiate equally in all directions are called omnidirectional and can only exist when the radiating structure is a point charge. Generating a point charge becomes a difficult problem when one considers the method for feeding this point charge will in turn disqualify it as such. Therefore, antennas such as a monopole and dipole, which exhibit somewhat equal spherical radiation patterns, are deemed omnidirectional. On the other hand, antenna structures which are designed such that the propagating wave is focused in a specific direction are called directional antennas. These become electrically larger than omnidirectional antennas and include horn and patch antennas.

Evaluation of the field distribution surrounding the conductor is oftentimes easier to analyze in the far-field of the structure where the propagating wave front becomes planar. This approach involves the development and evaluation of Green's functions through a volumetric integral. The results on the far-field analysis are then organized into well-known performance benchmarks such as gain, efficiency, beamwidth, and axial ratio [3]. Categorizing the trends in

7

antenna performance across frequency leads to distinction between resonant and frequency independent antennas.

Resonant antennas have a relatively small frequency region for which they exhibit favorable characteristics. Establishing some fraction of a wavelength along the conductor, they present the feed point of the antenna with a frequency dependent impedance due to the variations in the voltage and current. Therefore, the ability to impedance match across frequency becomes the limiting factor. The dipole antenna is comprised of two conductive traces extending away from the balanced feed point until the overall length becomes $\lambda_g/2$. At this length the impedance of the feed point is 73 +j42.5 Ω. The patch antenna is also designed to establish $\lambda_g/2$ along the conductor though feeding techniques can vary [3], [5][3]. Figure 2.1 shows the resonant current distribution of these antennas. The narrowband nature of resonant antennas allows them to be selective of the frequency content that is passed to the RF front end making them robust to out of band interfering signals. Advanced feeding techniques, such as using coupled lines to feed a patch antenna, further increase the amount of out of band rejection that is achieved [6]. This effort allows the receiver to be simplified by reducing the need for robust filtering and image frequency suppression [7].

Far-field analysis of a properly designed dipole antenna oriented along the z-axis in the cylindrical coordinate system results in the electric and magnetic fields shown in equations (2.1) and (2.2), respectively [3]. These equations describe a radiation pattern that is independent of ϕ and has a maximum at $\theta = \pi/2$, often described as a donut shaped pattern. Parallels can be drawn between the orthogonal relationship between the direction of peak radiation and the plane containing the conductors and extended to the loop and patch antennas shown in Figure 2.1.

8
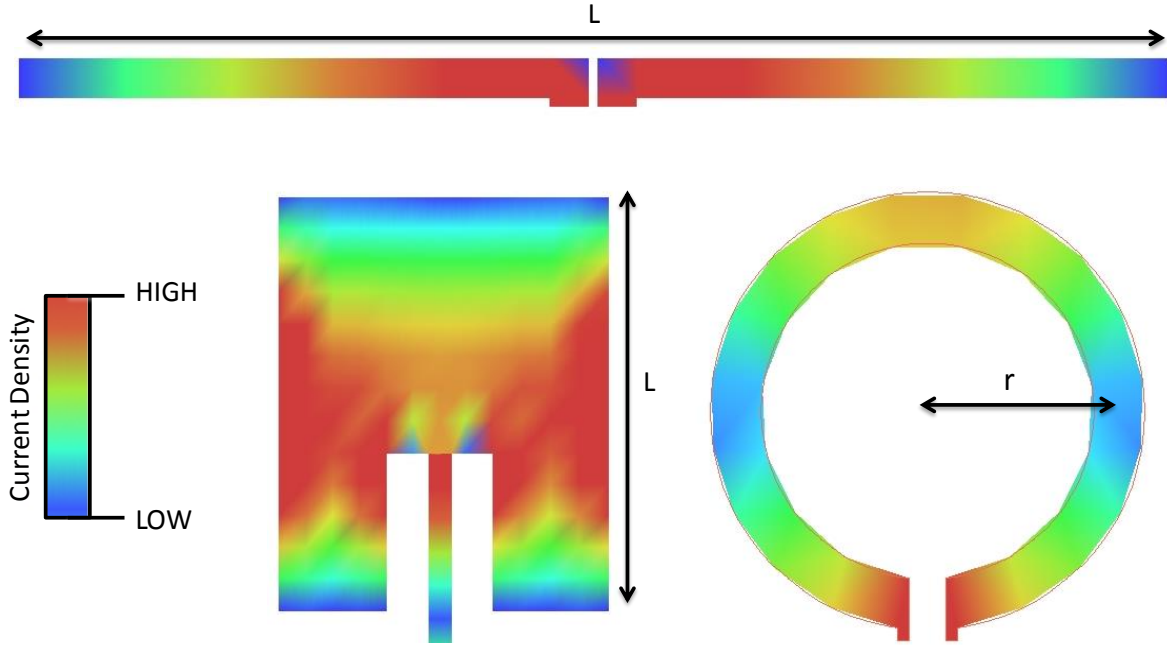
Figure 2.1. Current distribution of dipole (top), patch (bottom left), and loop antenna (bottom right). Reprinted with permission from [4].

$$E_\theta \cong j\eta \frac{I_0 e^{-jkr}}{2\pi r} \left[\frac{\cos\left(\frac{\pi}{2}\cos\theta\right)}{\sin\theta} \right] \tag{2.1}$$

$$H_\phi \cong j \frac{I_0 e^{-jkr}}{2\pi r} \left[\frac{\cos\left(\frac{\pi}{2}\cos\theta\right)}{\sin\theta} \right] \tag{2.2}$$

Frequency independent antennas are a classification of antennas that are specified by angles, are inherently broadband, and in theory scalable to any range of frequencies by an inverse scaling of physical size [3]. Equation (2.3) describes the shape of an equiangular spiral antenna, where *r* is the radius from the feed point of the spiral. The frequency independent nature of this category extends to characteristics such as polarization, gain, return loss, and radiation pattern making them candidates for ultra-wideband systems. Implementing a frequency independent antenna into a system capable of processing a broad range of frequencies introduces the capability

for multi-purpose radios. Due to the operational bandwidth of the antenna, care must be taken to avoid and mitigate against interfering signals. The previously mentioned benefit of resonant antennas does not translate to frequency independent antennas therefore proper characterization of the RF environment must be done and the burden of mitigation is placed on the RF front end. More information on this will be provided in further sections as addressing this issue is the pinnacle motivation for entirety of this work. Many ultra-wideband antennas, such as the Archimedean spiral antenna shown in Figure 2.2, exhibit performance similar to the equiangular antenna but are not considered frequency independent since they do not follow the fundamental equation (2.3). More information on frequency independent antennas can be found in [3].

$$r = F(\theta, \phi) = e^{a\phi} f(\theta) \tag{2.3}$$

$$\text{where } a = \frac{1}{K}\frac{dK}{dC}$$
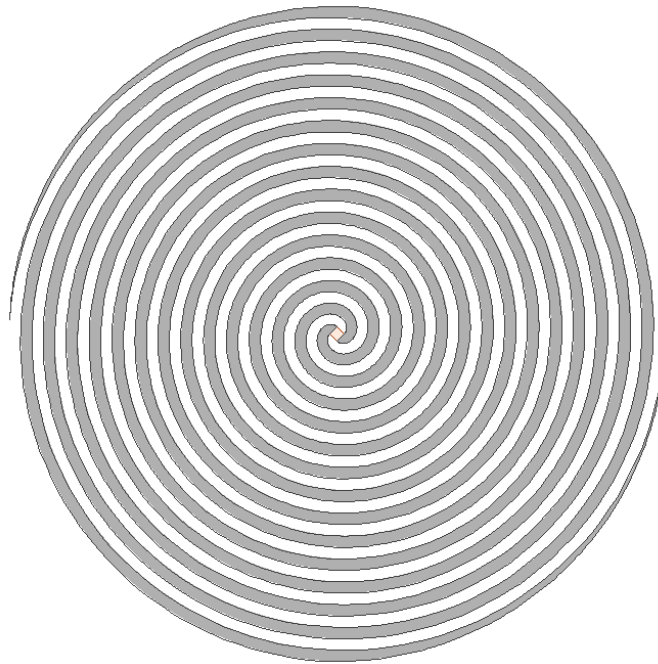
Figure 2.2. Layout of Archimedean spiral antenna. Reprinted with permission from [4].

10

2.2. Antenna Miniaturization Techniques

Antenna miniaturization has been a topic of research for decades and will continue to be a focus in applications where there is a desire to maximize performance in a size restricted system. Some of the most common published methods include increasing the permittivity surround the antenna through dielectric loading and meandering the conductive element to reduce its footprint [8] [9]. The impacts miniaturization of an antenna has on its performance are known to include reduced bandwidth, efficiency, and gain [3]. This section will investigate these two common techniques and help build a conceptual understanding.

As a wave propagates, whether is it in free space or in a guided manner, the velocity is impacted by the permittivity and permeability of its environment. The upper limit is set by the speed of light in a vacuum and decreases from there. If as an example we consider a transmission line of electrical length βl, increasing the permittivity will increase the electrical length by a factor of $\sqrt{\varepsilon_{eff}}$, see equation (2.4) [10]. When an antenna is placed on a dielectric substrate a similar phenomenon occurs. Figure 2.3 shows an edge fed patch antenna mounted on a dielectric substrate of thickness d and relative permittivity ε_r. Balanis presents a transmission line model to determine the length of a resonant rectangular patch by representing the patch with two slots separated by a distance of low impedance [3]. The effective permittivity (ε_{eff}) is calculated and used to account for the fringing fields which cause the aperture to appear larger than it physically is. To increase the effective permittivity surrounding the antenna the height of the substrate (d) can be increased, a material with a higher relative permittivity (ε_r) can be used, or a substrate and superstrate can be implemented [11]. Explaining dielectric loading with a lumped element transmission line model, as shown in Figure 2.4, can be done with a variation in capacitance per unit length where the velocity is calculated by equation (2.5) and the impedance of the line is calculated by equation

11

(2.6). Dielectric loading is known to come at the expense of reduced peak gain and bandwidth as more energy is trapped in the capacitive region between the patch antenna and ground plane.

$$\beta l \; = \; k_0 \, l \, \sqrt{\varepsilon_{eff}} \tag{2.4}$$
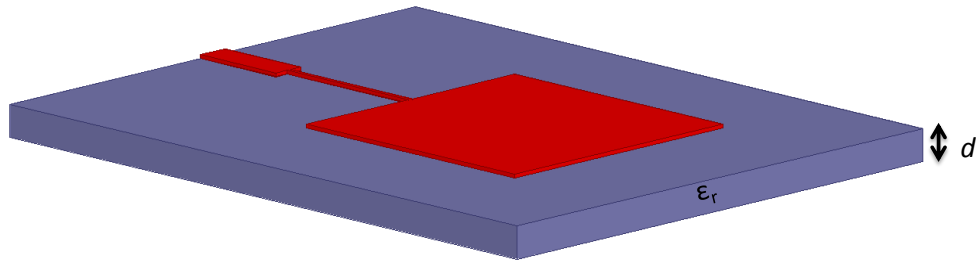
Figure 2.3. Example of a patch antenna loaded with a dielectric substrate of permittivity, ε_r, and thickness, d. Reprinted with permission from [4].

$$v_p \; = \; \frac{1}{\sqrt{L\,C}} \tag{2.5}$$

$$Z_o \; = \; \sqrt{\frac{L}{C}} \tag{2.6}$$
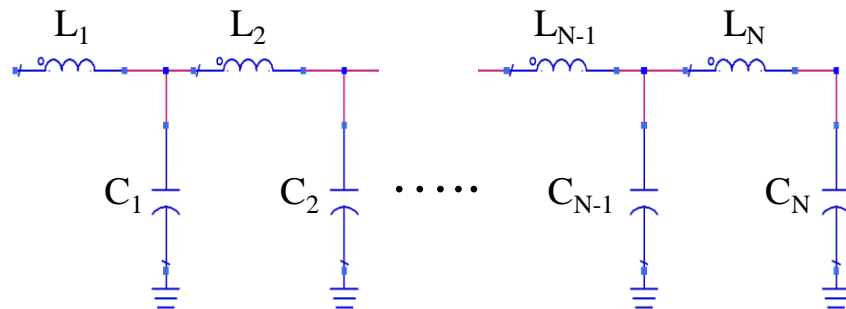
Figure 2.4. Equivalent circuit model of lossless transmission line. Reprinted with permission from [4].

Further reduction in the physical size of an antenna can be achieved by meandering the conductor of the antenna. This is best understood with resonant antennas where the bounding region enclosing the antenna is reduced by changing the shape of the conductor to occupy more of the central region. Figure 2.5 shows this being implemented with a loop antenna with an example of this done to a line antenna in [12]. Meandering antenna elements has been referred to as inductive loading in a lumped element transmission line model. This is done by considering the increase in the inductive transmission line along a projected length as opposed to the actual path length of the conductor. A direction relationship between the correlation of a lumped element model and antennas is exploited by using an artificial transmission line. Artificial transmission lines use a series inductor and shunt capacitor in a unit cell that is then cascaded demonstrating the ability to control both the velocity of propagation and impedance [13].
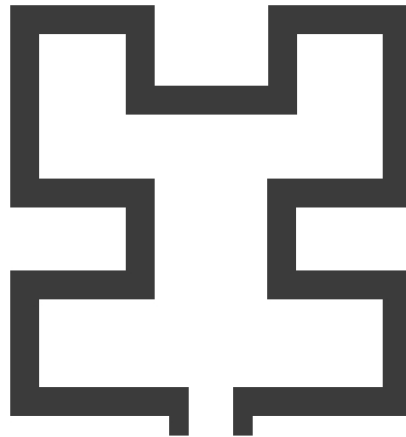
Figure 2.5. Layout of planar meandered loop antenna. Reprinted with permission from [4].

2.3. Miniaturization Limits

Both dielectric loading as well as meandering have proven to be effective methods to miniaturize an antenna at the expense of gain and bandwidth. The quality (Q) factor of an antenna

13

is proportional to its bandwidth and research has demonstrated the correlation between electrical size (ka) and Q-factor. An electrically small antenna was defined in 1947 by Wheeler as one that has a volume smaller than the radian sphere, where the radian sphere has a radius (a), as defined in Figure 2.6, of $\lambda/2\pi$ [14]. The correlation between ka and bandwidth was furthered and published as the Chu Limit. The Chu limit models a single mode of an antenna as either an inductor or capacitor along with a resistor to derive spherical wave functions and arrive at a minimum quality factor shown in equation (2.7) [15]. Mclean provided a simplified version of the Chu limit and stated that for antenna for which $ka \ll 1$ the quality factor is inversely proportional to the cube of ka [16]. Figure 2.7 plots the minimum achievable quality factor as a function of electrical size using equation (2.7). More information on an antennas quality factor can be found in [17].

$$Q = \frac{1+2\,(ka)^2}{(ka)^3\,[1+(ka)^2]} \quad for \; ka \ll 1 \; Q = \frac{1}{(ka)^3} \tag{2.7}$$
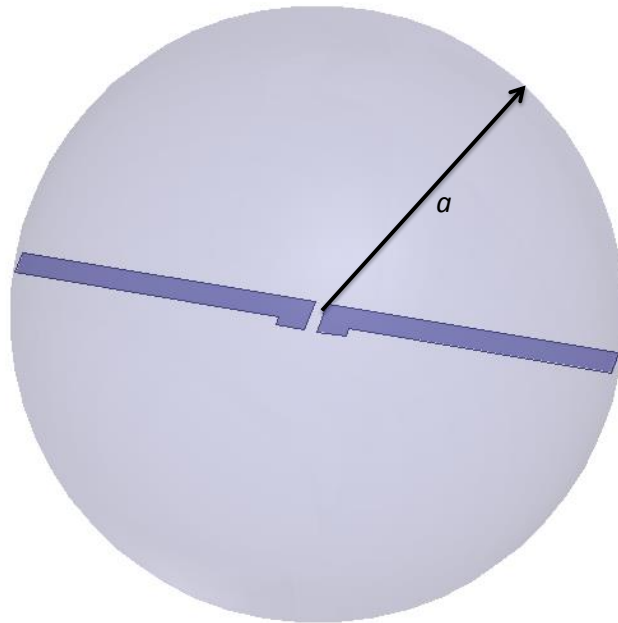
Figure 2.6. Sphere containing the antenna where *a* is the radius of the sphere. Reprinted with permission from [4].

14
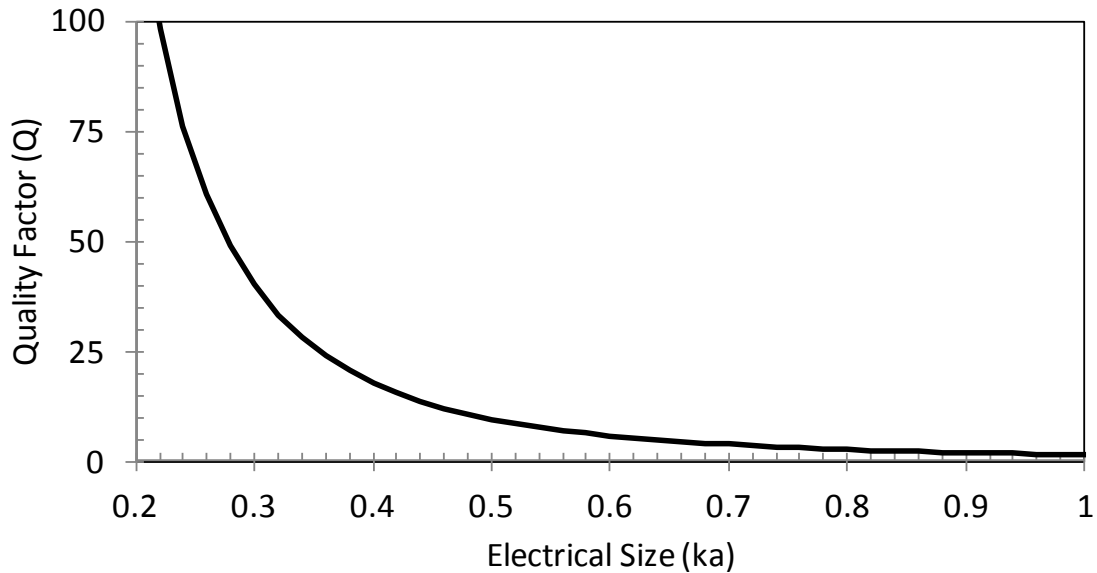
Figure 2.7. Theoretical quality factor limit versus antenna size. Derived from [14]. Reprinted with permission from [4].

2.4. Interference Mitigation Techniques

In a typical RF environment, unwanted signals are available at the antenna interface which, if not properly accounted for, will increase the noise floor of a receiver and potentially cause damage to the RF front end. These additional, unwanted, sources can be friendly or hostile and have been exploited to jam receivers rendering them ineffective. This ineffectiveness can come about by either increasing the noise floor to a point where the intended signal is no longer able to be properly demodulated or pushing the front end low noise amplifier (LNA) into compression causing distortion. Placing the front-end filter prior to the LNA can help mitigate compression due to adjacent, interfering signals at the expense of increased system loss and therefore receiver noise figure. If the front-end filter is placed after the LNA the interfering signal can still be attenuated prior to the demodulator but the LNA will remain unprotected, see Figure 2.8.

The noise floor of a receiver is typically calculated assuming a rectangular shaped bandwidth with infinite out of band rejection. Alternatively, the measured frequency response of

15

the front-end filter can be integrated to account for finite band edge performance resulting in an effective noise bandwidth, which results in a higher calculated noise floor [18]. When an interfering signal is present close to the band edge of the filter the non-ideal rejection must be accounted for to properly characterize the receiver.
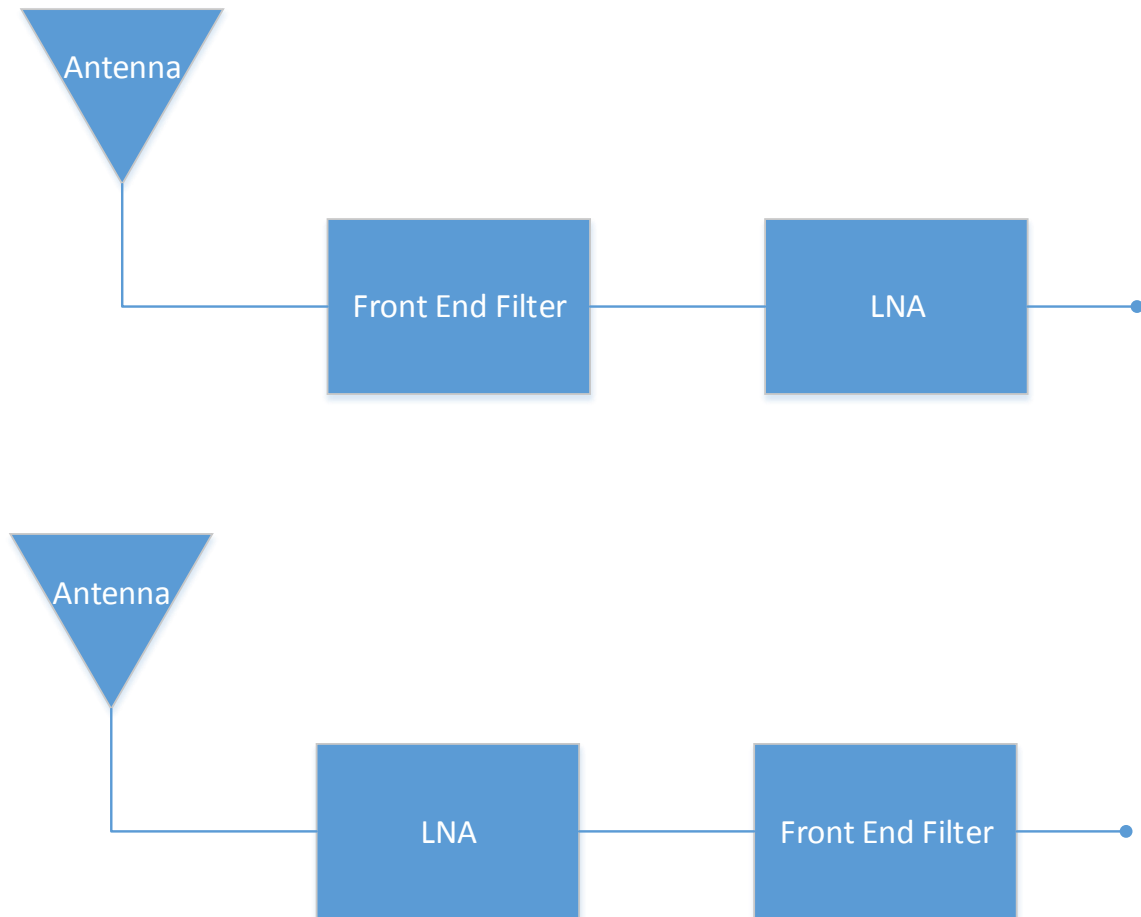
Figure 2.8. Example RF front end showing filter prior to LNA (top) and filter after LNA (bottom).

With the goal of attenuating known interfering signals in ultra-wideband systems, filtering structures have been integrated directly into the antenna resulting in the ability to reduce the gain at a particular frequency. Placement of resonant structures within the radiating aperture oftentimes

16

achieves 10 dB of attenuation with respect to the nominal gain. Capacitive loaded loop resonators couple to the feed line of a disc monopole antenna resulting in 9 dB of reduced gain. Increasing the number of resonators in the disc monopole to three demonstrates the ability to generate separate rejection bands [19]. A U-slot placed directly into the radiating aperture of a wideband monopole obtains 11 dB of gain reduction [20]. To date the best known rejection achieved from integrating resonant structures into an antenna has been reported using ultra-wideband dipole antennas and creating elliptical voids into each arm of the dipole. This work measured six different designs, each with a different notch resonant frequency, with the highest achieved gain reduction being 29.4 dB [21]. Multiple studies demonstrate different configurations of resonators integrated into various antenna structures but there has been no known investigation to the optimal placement of these resonators.

If system requirements permit the implementation of two antennas adaptive cancellation becomes an attractive technique for interference cancellation. Adaptive cancellation systems, such as the one shown in Figure 2.9, require a receive antenna that accepts both the signal of interest and the interfering signal as well as a reference antenna that ideally accepts only the interfering signal. The interfering signal is then coupled into the receive line through a 180 degree coupler with the intention of reducing the power level of the interfering signal while leaving the intended signal unaffected. A subsequent coupler is used to monitor any phase error present and fed back into the adaptive canceller to optimize the achieved cancellation. System level considerations come into play as to whether the adaptive cancellation occurs at the RF of IF stage and the location of the local oscillator. This approach is effective for out of band signals, as shown in Figure 2.10, but does little to address in-band interference. More information on advanced implementations of adaptive cancellation can be found in [22].

17
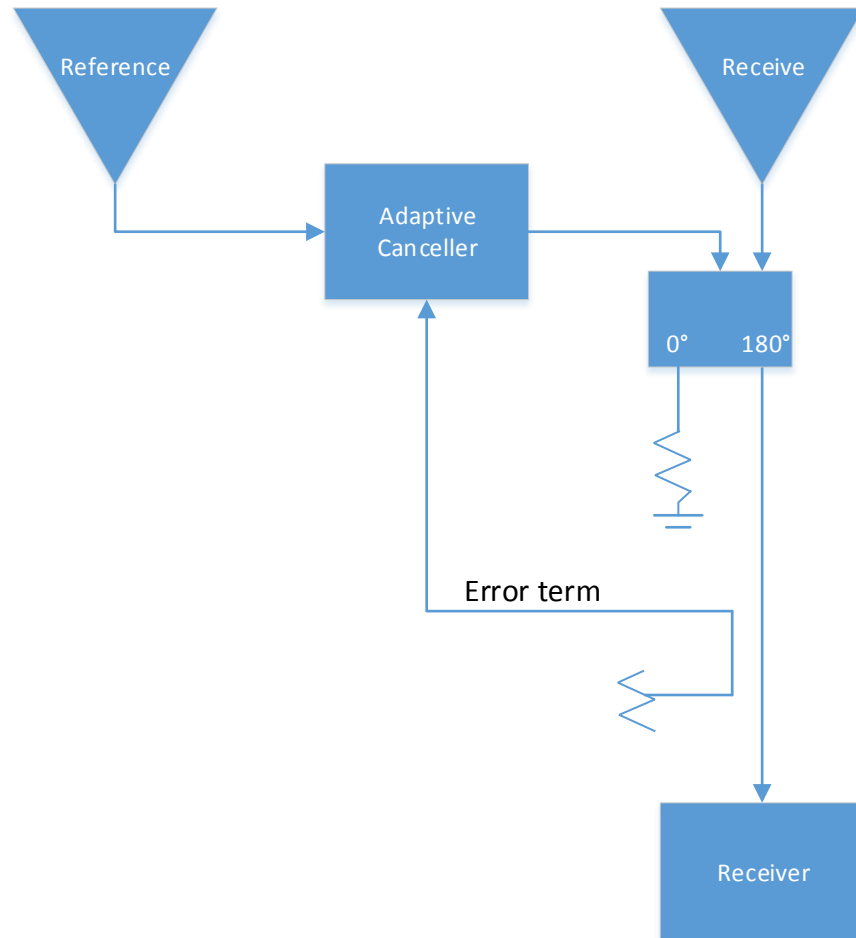
Figure 2.9. Block diagram of adaptive cancellation system.
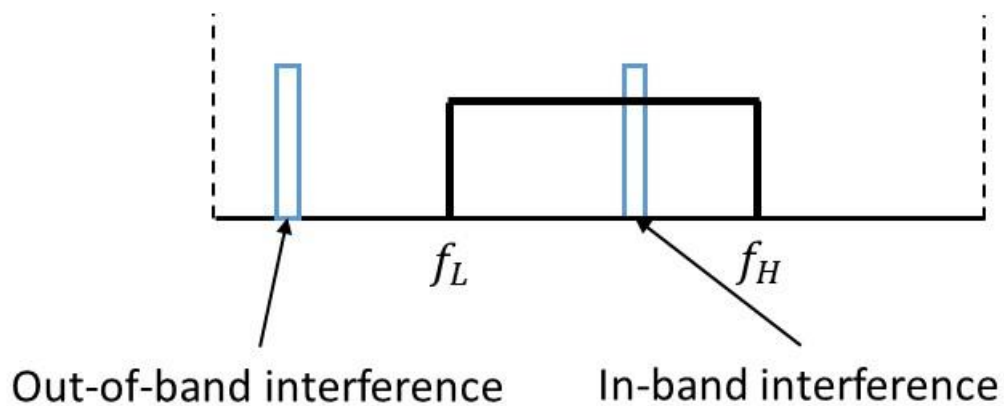
Figure 2.10. Pictorial description of intended operational bandwidth ranging from f_L to f_H in the presence of an out-of-band as well as in-band interference.

18

2.5. Conclusion

The design and miniaturization of antennas requires an understanding of the electromagnetic fields on the antenna structure. A $\lambda/2$ dipole antenna has a current maximum at the feed point of the antenna and decays to a minimum at the ends. This behavior controls parameters such as input impedance, radiation pattern, and directivity. To miniaturize the design this chapter explored two common planar techniques, capacitive and inductive loading, which come with a tradeoff in decreased antenna performance. Due to the relationship between quality factor and sphere size (ka) defined by Chu higher efficiency miniaturization can be achieved by using all three dimensions during the design process.

CHAPTER 3: PERIODIC SPIRAL ANTENNA DESIGN AND MODELING

3.1. Periodic Spiral Antenna Design

This chapter describes the general design, prototype fabrication, and performance summary of the periodic spiral antenna. The theoretical concept is described in detail in [2] and is summarized here for convenience. Copyright permission is given in Appendix C.

There are many configurations for the construction of a spiral antenna. These configurations include the Archimedean, equiangular, and sinuous spiral. Each these designs can be implemented with one, two, or four arms and with a planar or conical shape [3]. Radiation of these spiral antennas occurs by exciting a traveling wave along the arms of the spiral. More specifically, a two-arm spiral is fed with a signal of equal amplitude and a phase shift of 180° between arms. As the signal propagates the currents of the adjacent arms begin to align in phase creating constructive interference in the far-field leading to radiation. The radiation band of a spiral antenna is frequency dependent and occurs roughly in a region that is λ_g in circumference. Therefore, the high frequency limit of a spiral antenna is limited by the resolution of the inner turns and the low frequency limit is determined by the outer circumference [23]. The ideal miniaturization of a spiral antenna will lower the low frequency operational point while leaving the high frequency radiation band unmodified. The traditional method for implementing such miniaturization is done with a tapered dielectric substrate with a height that is a function of radius therefore increasing the dielectric loading as the spiral antenna operational frequency decreases.

20

The periodic spiral antenna (PSA) is based on a two-arm Archimedean spiral architecture. Inductive loading of the arms is introduced by modulating the height of the element in a sinusoidal fashion as a function of angular distance. Figure 3. shows the configuration of the PSA where R is the radius, d is the spacing between arms, a is the amplitude of oscillation, W is the width of the conductor, and T is the period of oscillation. The shape of the PSA can best be described in cylindrical coordinates by equation (3.1) where $\vec{r}$ is the radius vector forming the antenna, G is the Archimedean growth rate, N is the number of oscillations per turn, and $f(\phi)$ is some function describing the amplitude growth profile.

$$\vec{r} = G\phi\,\hat{\rho} \; + \; f(\phi)\sin N\phi\,\hat{z} \tag{3.1}$$
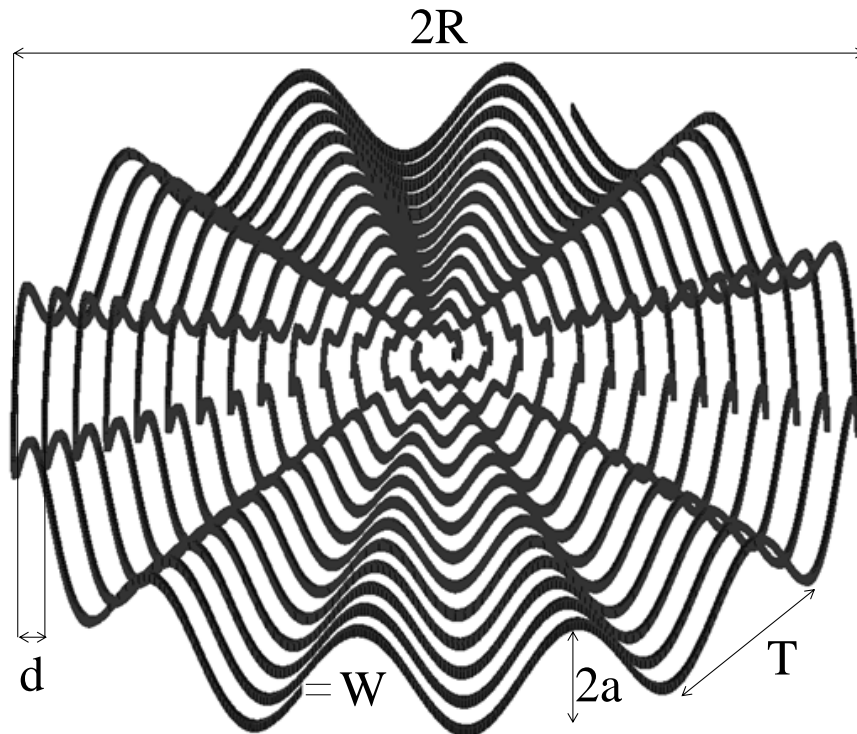
Figure 3.1. Isometric view of the periodic spiral antenna with a linear growth profile. Reprinted with permission from [2].

21

The introduction of the z-dimension as a design tool for an Archimedean spiral antenna allows additional miniaturization of the antenna element prior to dielectric loading. To better understand the relationship between all the design variables an equivalent circuit model is developed and design curves are published in [2].

An efficient fabrication approach for prototyping purposes was achieved with an additive manufactured substrate and 20 AWG copper wire. The substrate was printed on a Fortus 400mc using and ULTEM 1000 filament [24]. Additive manufacturing expedited the prototyping phase and reduced complications in generating the 3D features used in the PSA antenna. The balanced feed necessary to feed the PSA was achieved with a tapered microstrip balun fabricated on Rogers RO4360G2. More information on the design and performance of the microstrip balun can be found in Appendix A. The fabricated PSA with an exponential growth profile is shown in Figure 3.2. Measured results confirm an overall miniaturization factor of 1.5 while maintaining gain and return loss over a 3.75:1 bandwidth.

Figure 3.2. Fabricated model of sinuous cavity backed PSA antenna utilizing an exponential growth factor of 3.

22

3.2. Improvements to Fabrication Methodology

Given the complexity of the physical design, the prototype fabrication method exposed inconsistencies between units as well as an assembly time of approximately one hour per unit. The challenge with the prototype manufacturing process described in Section 3.1was primarily related to bending the wire to form the antenna element with the remainder of the assembly time totaling about 5 minutes.

The periodic spiral antenna achieves miniaturization by meandering the conductor in the z-axis increasing the inductance per unit length in a smooth transition while maintaining arm to arm capacitance throughout the structure. An alternative method for miniaturization has been published where the conductor width lies along the z-axis creating a parallel plate style of structure [25]. This arrangement was coined the "thick Archimedean spiral". Parametric studies were conducted that demonstrated trends between spiral arm geometry, such as arm to arm spacing and arm "thickness", and equivalent capacitance. These extracted parameters were then extended to a miniaturization factor for the thick Archimedean spiral and verified through full wave simulation. The most notable compromise for an increased miniaturization factor was a decreased input impedance due to the capacitive loading effects of a "thicker" arm. It will be shown that combining the miniaturization technique of the PSA along with that of the "thick Archimedean spiral" leads to a design that reduces assembly time and also provides a path for additional miniaturization of the PSA design.

The proposed assembly consists of a spiral arm that has a width in the horizontal plane of 1.4 mils and a vertical height of 80 mils. This conductor has the same dimensions as a transmission line realized with 1 oz. copper therefore it can be fabricated on a flexible circuit board. Assembly into a spiral consists of sliding the flex circuit down into a substrate which contains a slot to control

23

the Archimedean growth rate. With the configuration presented it can be thought of as the large dielectric substrate controlling the Archimedean growth rate and the conductor of the flex circuit controlling the amplitude growth profile. Repeatability and accuracy of this stage of assembly then becomes a function of dielectric machining tolerances and resolution of the wet etch process used to fabricate the copper strip on to the Polyimide flexible substrate.

The fabrication of the spiral arms is done on a 5 mil thick Polyimide substrate using 1 oz. copper. The thickness of the Polyimide substrate was found to not be critical from a radiation perspective so mechanical factors, such as bend radius and stiffness, were considered. A transform of the PSA design equations to a form suitable to be fabricated on a sheet is achieved with equations (3.2) and (3.3). Figure 3.3 shows multiple spiral arms fabricated of a single substrate which are subsequently cut out for installation. The ability to batch produce the spiral arms contributes to the low manufacturing cost of this design.

The body of the dielectric has also been redesigned to accommodate the new configuration of the spiral arms. The sinusoidal shape on the top of the dielectric shown in Figure 3.2 is no longer necessary and is changed to a flat surface, which removes sharp points that are hard to manufacture reliably with the 3D printer. The groove now has a constant 10 mil width in the x-y plane and increases in depth radially to match the amplitude of the spiral arms. To demonstrate manufacturability the dielectric height was reduced to 400 mils to remove unnecessary material and 3D printed with Polycarbonate on a Fortus 400mc. A photo of the demonstration dielectric containing a single spiral arm fabricated on 5 mil Polyimide with 1 oz. copper is shown in Figure 3.4. In this figure the spiral arm is partially installed whereas the fully installed arm would lie flush with the top of the demonstration dielectric.
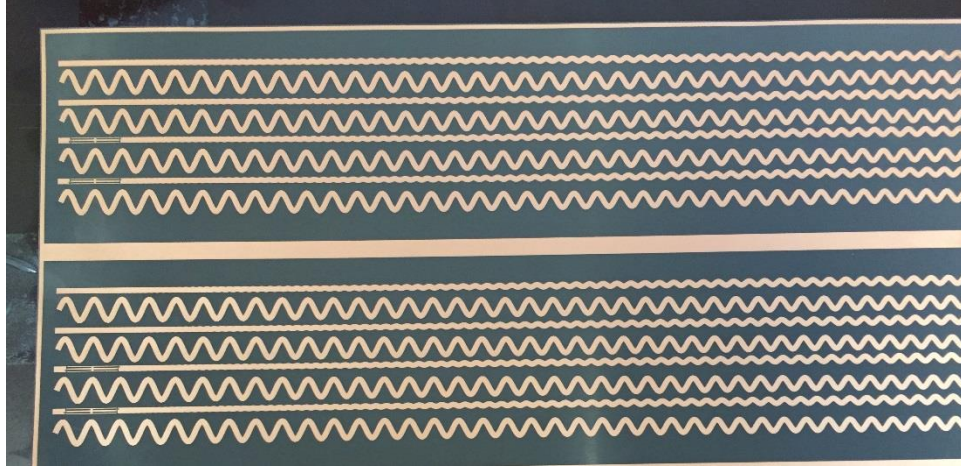
Figure 3.3. Multiple PSA elements fabricated on 5 mil Polyimide using a wet etch process.

$$X = \frac{G}{2}\left(\phi\sqrt{1 + \phi^2} + \sinh^{-1}\phi\right) \tag{3.2}$$

$$Z = f(\phi)\sin(N\phi) \tag{3.3}$$

Figure 3.4. Additive manufactured Polycarbonate dielectric with PSA element partially installed.

3.3. Equivalent Transmission Line Model

The benefit of an equivalent transmission line model lies in its ability to understand the fundamental operation of an antenna. For a spiral antenna currents in adjacent arms change their phase relative to each other as the signal propagates towards the tip of the arms [23]. When a wave is launched into the feed point of a two arm spiral an odd mode current distribution is generated. The time variant signal is slowed down prior to the radiation band and the location of such radiation is established by the odd mode phase velocity of the signal. An equivalent transmission line model can help to understand the location of fields to better utilize dielectric loading and other miniaturization techniques to aid in the reduction of the odd mode phase velocity.

A two-arm spiral antenna is fed in a balanced configuration and therefore in this region currents on adjacent arms flow in opposite directions causing cancellation in the far-field. Consider a section of the spiral in the non-radiating region: in this section a particular conductor will have currents that flow in the clockwise direction, the center conductor, while the conductors adjacent to it, both closer to and further from the center, will have currents that flow in the counterclockwise direction, the ground conductors. This current distribution is shown in Figure 3.5 which shows a TEM style of propagation with the center conductor coupling to the ground conductors. The described field distribution and propagation is very similar to that of a stripline structure shown in Figure 3.6 where the center conductor is the signal path with the return path on either side exhibiting a surface current 180° out of phase. It will be shown in Chapter 4 that leveraging a stripline equivalent transmission line model can allow for simple filter design to be conducted separate from the antenna design resulting in decreased computational resources.
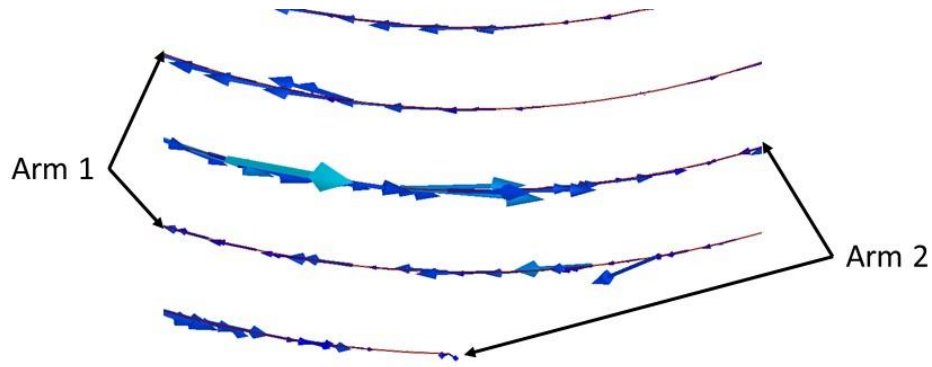
Figure 3.5. Surface current vectors in the non-radiating portion of a spiral antenna.
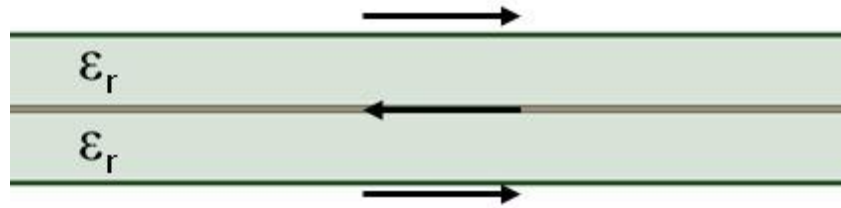
Figure 3.6. Surface current vector of stripline mode propagation.

3.4. Thermal Implications

Thermal considerations of a microwave structure must be taken into consideration during the design process when an appreciable power level is present. Some of the most common issues related to power handling of the structure include voltage breakdown and thermal generation leading to fluctuations in relative permittivity and phase transition of the substrate. Thermal modeling of the antenna structure can be a useful tool in identifying locations of heat generation and understanding the impact of dielectric parameters, such as loss tangent, in reducing the thermal load. ANSYS Workbench provide a simulation platform that combines the high frequency simulation capability of HFSS with the steady state thermal simulation available with Mechanical. This platform was used to study thermal generation along the balun and results are published in [4].

27

Thermal conductivity (k) is a material property that governs the rate of heat transfer inside the volume of a material [26]. The rate of heat transfer within the volume of a material is governed by the law of thermal conduction. Equation (3.4) describes how energy moves through a volume where A is the cross-sectional area of a mesh within the volume, $|dT/dx|$ is the temperature gradient between meshed cells, and $\wp$ has units of watts. The quantitative explanation for the boundary condition that is encountered between the surface of the volume containing the heat source and air is described by Newton's Law of Cooling [26]. This law is described with equation (3.5) where h_c is the convective heat transfer coefficient and dT is the temperature difference between the surface of the volume and the surrounding environment.

$$\wp = kA \left|\frac{dT}{dx}\right| \tag{3.4}$$

$$q = h_c\, A\, dT \tag{3.5}$$

Conservation of energy states that energy cannot be created or destroyed, but can be transitioned from one form to another [27]. More specifically, the electrical energy lost during propagation is transformed into thermal energy. To simplify this to an example a two-wire transmission line can be considered. Transverse electromagnetic (TEM) propagation along a transmission line is explained with Telegrapher's equations shown in (3.6) through (3.9) [10]. The power loss along a transmission line is the difference between the accepted power and the power delivered to the load and can be described by equation (3.10) where Γ is the reflection coefficient. If the structure contains a finite loss the complex propagation constant (γ) consists of two components, an attenuation and phase constant, as shown in equation (3.8). Further decomposition

28

of the real part of the propagation constant shows that the attenuation constant of the wave is comprised of three individual loss factors; conductor loss (α_c), dielectric loss (α_d), and radiation loss (α_r) as shown in equation (3.9). Properly designed transmission lines have minimal radiation loss while antenna structures exhibit significant radiation loss and must be accounted into the attenuation of the wave along the transmission line. In either case, the nature of radiation loss does not contribute to thermal generation since the electrical energy is transitioned from a guided to an unguided form of propagation. Alternatively, the conductor and dielectric losses lead to a transition from electrical to thermal energy. To minimize thermal generation on a microstrip line a low loss, low permittivity substrate with a wide, high conductivity conductor should be used. Additional information on thermal trends in microstrip structures can be found in [4].

$$V(z) = V_o^+ e^{-\gamma z} + V_o^- e^{\gamma z} \tag{3.6}$$

$$I(z) = I_o^+ e^{-\gamma z} + I_o^- e^{\gamma z} \tag{3.7}$$

$$\gamma = \alpha_t + j\beta \tag{3.8}$$

$$\alpha_t = \alpha_c + \alpha_d + \alpha_r \tag{3.9}$$

$$P_{loss} = P_{in} - P_L = \frac{|V_o^+|^2}{2Z_o}[(e^{2\alpha l} - 1) + |\Gamma|^2(1 - e^{-2\alpha l})] \tag{3.10}$$

Orienting the conductor for the antenna element along the z-direction allows for a higher level of miniaturization due to the increased capacitance per unit length. Similar to a parallel plate

capacitor, the fields surrounding the conductors are concentrated between the arms of the PSA in the non-radiating region. The same concentration of fields that aids in the miniaturization of the PSA results in an increased power loss density residing in the dielectric substrate which will translate to a higher thermal generation. ANSYS HFSS can directly plot power loss density to quantify the relationship between loss tangent and thermal generation in a radiating structure. This plot signifies the location and magnitude of the losses but does not account for the thermal conductivity of the material and the boundary conditions necessary to calculate an absolute temperature.

A cross section view of the power loss density residing in the dielectric at 1.2 GHz is shown in Figure 3.7. Immediately noted is the location of the largest loss occurring between the adjacent arms towards the center of the spiral. Comparatively, power loss density in the dielectric region between the spiral arms and the conductive cavity is substantially lower. Another region of diminished loss density resides between the spiral arms roughly half of the distance between the center of the spiral and the outside of the dielectric. Figure 3.7 also shows another cross section view with the plane of view intersecting the spiral arms. Following the direction of the spiral arms, the same pattern is observed where a high loss density occurs towards the center of the spiral, followed by a diminished loss density, and finished with a slightly increased loss density. To better describe this phenomenon the power loss density is plotted along with the surface current vector of the conductors and shown in Figure 3.8. As a refresher, the radiating region of the spiral antenna occurs when adjacent arms have in phase currents and therefore the concentration of electric field potential in the dielectric substrate between adjacent arms approaches zero. Figure 3.8 shows a correlation between these in phase currents residing on the spiral arms and the diminished power loss density within the dielectric. Extending this to other frequencies simply entails understanding

30

the theory of operation for spiral antennas. More specifically, an understanding of the location of the radiation region and prior to this region the largest power loss density will reside. Therefore, it would be expected to see a concentration of thermal energy towards the center of the antenna for most of the frequencies of interest for this antenna.
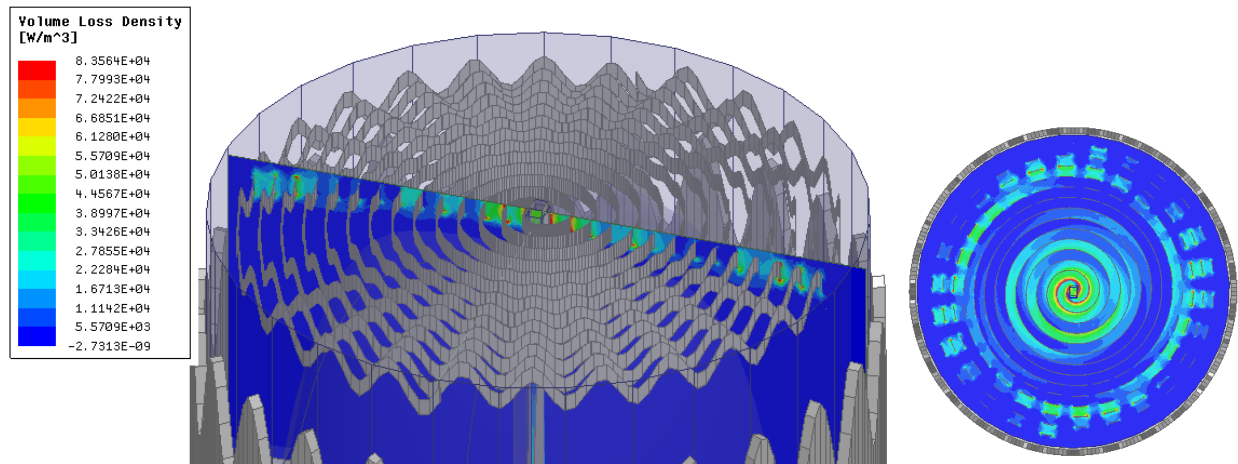
Figure 3.7. Power loss density plotted at 1.2 GHz with 1 W of incident power.
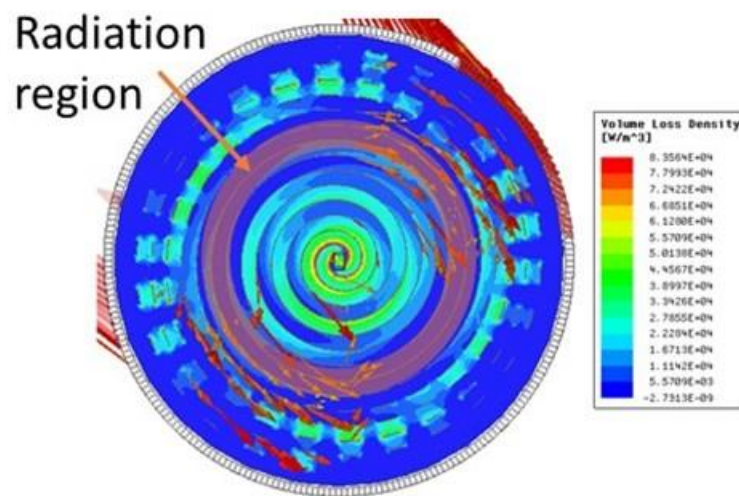
Figure 3.8. Power loss density within the dielectric and surface current vectors on the spiral arms plotted at 1.2 GHz with 1 W of incident power.

31

The power loss density in the dielectric substrate is a function of the loss tangent of the material. With the proposed configuration of the spiral arms the concentration of fields in the dielectric in the non-radiating portion impose a high level of importance on dielectric loss tangent. Figure 3.9 plots the power loss density along a line traveling radially from the center of the spiral to the outside of the dielectric. Large discontinuities are attributed to the boundary condition between dielectric and conductor as the line passes through. The point 2.6 cm from the center of the spiral exhibits an 11.3 times larger power loss density when increasing the dielectric loss tangent from 0.0006 to 0.01. This does not translate directly to an 11.3 times higher temperature but does correlate to thermal generation in the dielectric.
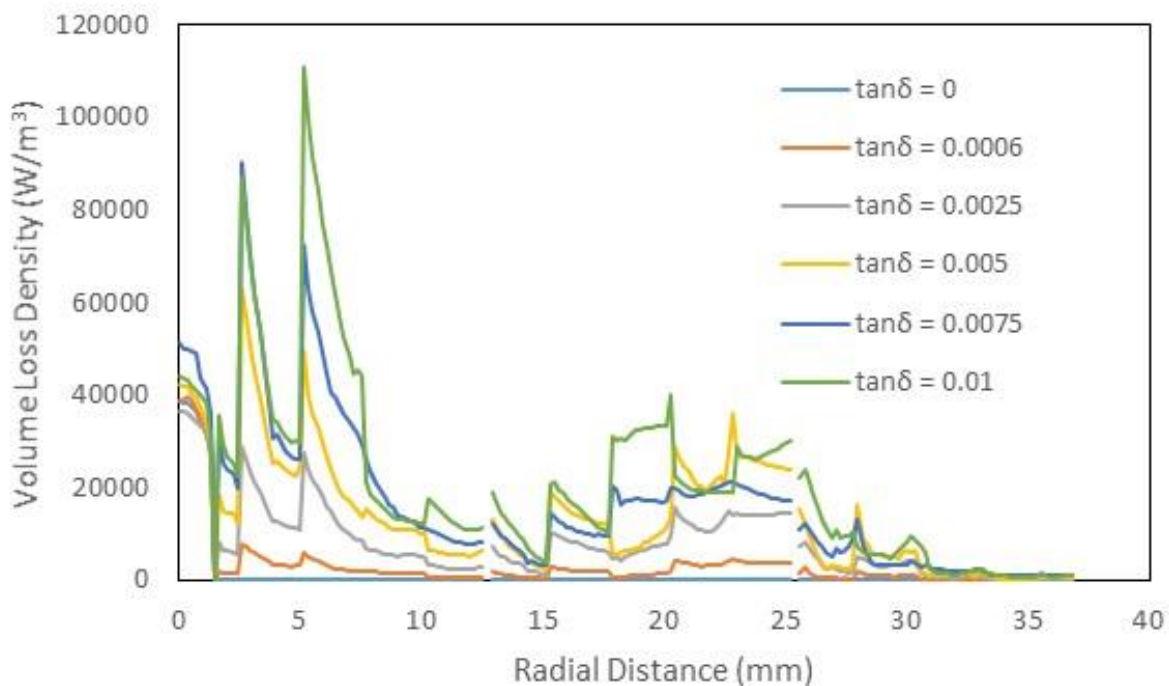
Figure 3.9. Power loss density plotted as a function of loss tangent at 1.2 GHz with 1 W of incident power.

32

3.5. Thermal Measurements

Thermal measurements were conducted to quantify temperatures experienced during conditions of high incident power. The cavity backed periodic spiral antenna, shown in Figure 3.10, was placed inside a screen room with all electronic equipment placed on the outside. Absorbing cones were arranged to attenuate the radiated power and reduce reflections inside the Faraday cage. An Agilent 8648C signal generator was used to feed an Amplifier Research model 100S1G6AB 1 – 6 GHz 100 W high power amplifier (HPA). A coaxial cable was used to route the output of the HPA to the connector of the periodic spiral antenna with a 40 dB dual-directional coupler placed inline and with the coupled port connect to an Agilent E4417A power meter. A diagram of the test configuration is shown in Figure 3.11. The insertion loss of this coaxial cable and the through path of the dual-directional coupler was measured to account for the power loss between the two units using equation (3.11). RF power was applied to the PSA for a minimum of 20 minutes, which was the longest time it took the temperature to reach steady state. To avoid potential damage, the thermal camera was kept outside of the screen room during high power RF transmission and thermal images were taken as quickly as possible after the RF power was turned off using a FLIR T621xx. To accurately measure temperature using an IR camera the emissivity of the object being imaged must be known. The emissivity of an object is its ability to emit infrared energy. Emissivity is ranked from 0 to 1.0 with 0 being a shiny mirror and 1.0 being a blackbody radiator [26]. Therefore, if the emissivity of the object being imaged is incorrectly stated at 0.5 instead of 0.9 the calculated temperature based on the detected IR radiation will be higher than the

33

actual temperature. A series of measurements conducted by NASA at the Goddard Space Flight

Center revealed the emissivity of machined bulk ULTEM-1000 ranging from 0.897 to 0.899 [28].

Figure 3.10. Cavity backed periodic spiral antenna.
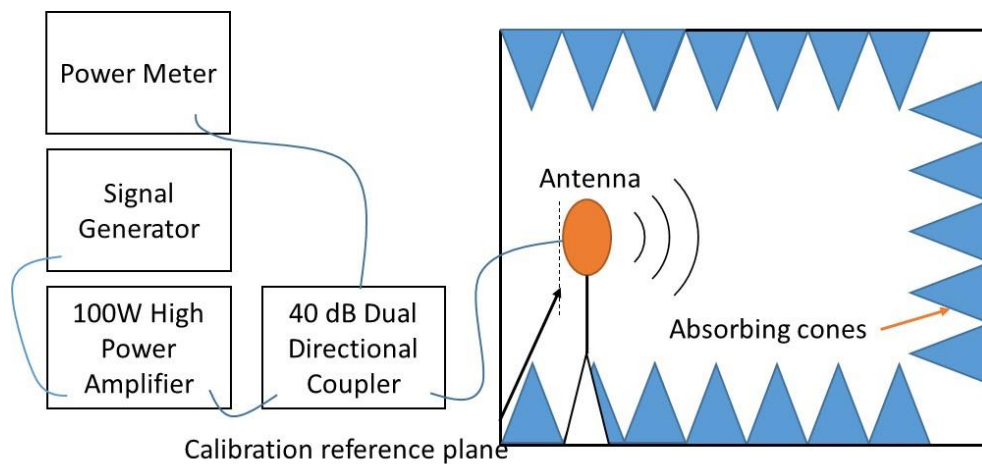
Figure 3.11. Diagram of high power test configuration.

$$Power_{PSA} = Power_{HPA} * 10^{S_{21}/10} \qquad (3.11)$$

Thermal images are taken using a cavity backed PSA with an additive manufactured ULTEM 1000 dielectric and spiral arms that are fabricated on a 5 mil thick Polyimide substrate. The balun material is Rogers RO4360G2 with 1 oz. copper. The reflection coefficient was measured using an Agilent E5071C vector network analyzer with the measurement reference plane placed at the SMA connector of the antenna using a 1-port short, open, load calibration. Results of this measurement at frequencies of interest are shown in Table 3.1. A summary of the peak recorded temperatures at 1, 2, and 3 GHz with an incident power of 10 to 60 watts is reported in Table 3.2. This data shows an increase in temperature with rising incident power levels as increasing frequency. When 50 W of incident power was applied at 3 GHz the ULTEM substrate melted and the solder disconnected the spiral arms from the balun causing failure of the antenna. A image of the failure point is shown in Figure 3.12. As previously described with Figure 3.7 and Figure 3.8 the largest expected thermal load will be towards the center of the spiral and bound inside the circumference of the radiation region. Figure 3.13 shows a detailed thermal image for each incident power and frequency measured. As predicted by the current loss density plots, the highest temperature occurs close to the feed of the spiral. The area of the largest thermal load appears to have a frequency dependent nature with it decreasing in diameter with increasing frequency. This relationship corresponds to the smaller circumference radiation band required as frequency increases, which is depicted in Figure 3.14 where the radiation band is highlighted for the same frequency as the thermal measurement.

Table 3.1. Measured return loss and calculated accepted power levels at frequencies measured during high power testing.

	10 W	20 W	30 W	40 W	50 W	60 W
1 GHz Return Loss (dB)	-8.9	-8.9	-8.9	-8.9	-8.9	-8.9
1 GHz Accepted Power (W)	8.7	17.4	26.1	34.8	43.6	52.3
2 GHz Return Loss (dB)	-9.2	-9.2	-9.2	-9.2	-9.2	-9.2
2 GHz Accepted Power (W)	8.8	17.6	26.4	35.2	44.0	52.8
3 GHz Return Loss (dB)	-15.5	-15.5	-15.5	-15.5	-15.5	-15.5
3 GHz Accepted Power (W)	9.7	19.4	29.2	38.9	48.6	58.3

Table 3.2. Maximum measured steady state temperatures for the cavity backed PSA for a range of frequencies and incident power levels.

Incident Power (W)	Measured temperature at 1 GHz (°C)	Measured temperature at 2 GHz (°C)	Measured temperature at 3 GHz (°C)
10	36	52	48
20	58	69	82
30	74	89	112
40	93	109	146
50	110	131	Fail
60	132	167	Fail

Figure 3.12. Damage incurred during thermal testing with 50 W incident power at 3 GHz.
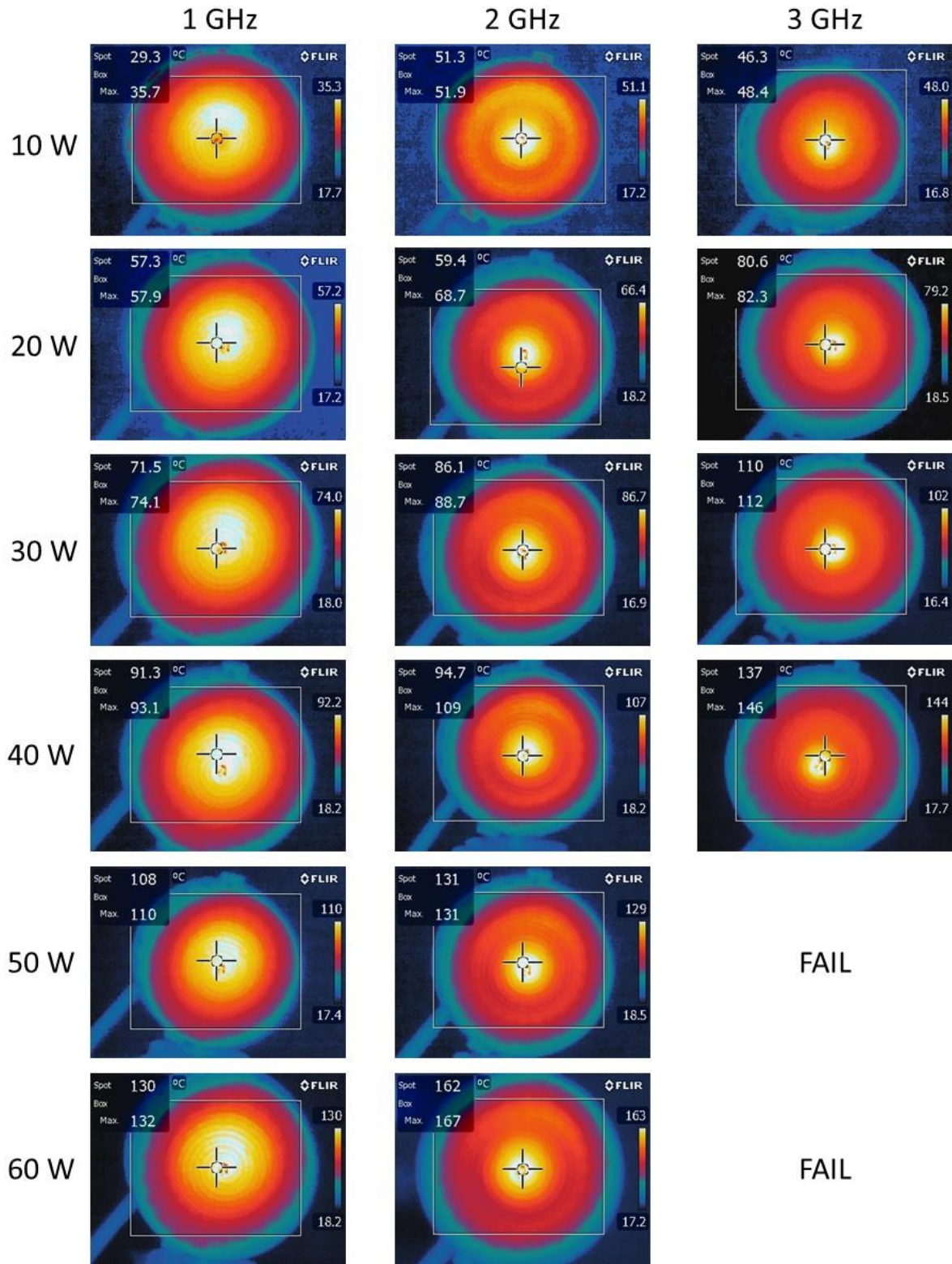
Figure 3.13. Measured steady state thermal images for the cavity backed PSA for a range of frequencies and incident power levels.
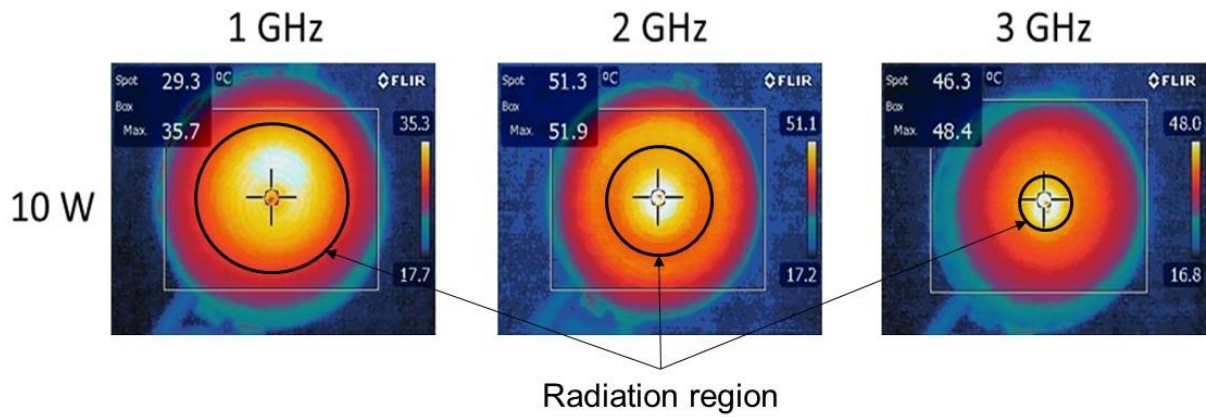
Figure 3.14. Measured steady state thermal images for the cavity backed PSA highlighting the radiation region based on thermal profile.

CHAPTER 4: INTERFERENCE REJECTION IN ULTRA-WIDEBAND SYSTEMS

4.1. Introduction

While ultra-wideband antennas allow a single RF front end to handle multiple communication protocols they are also susceptible to high power jamming signals. These interfering signals may be hostile or a collocated friendly signal. In either case, it is desirable to attenuate the unwanted high power signal prior to the RF front end to prevent damage or reduced receiver sensitivity. Historically, this has been addressed by placing additional filtering blocks between the antenna and the RF front end resulting in more components, increased loss, weight, and size [22].

To date there have been two main paths taken to include a rejection band into the frequency response of an antenna: incorporating a resonant structure into the radiation aperture or placing coupled resonators along the feed line for the antenna. Placing a resonator into the aperture of a wideband monopole has resulted in a rejection between 10 – 15 dB [29] – [31] while maintaining peak gain performance outside of the rejection band. Using resonators to couple to the feed line of a wideband monopole resulting in a rejection of 8.5 – 9 dB [32], [33]. It was also demonstrated here that multiple resonators could be incorporated into the structure but these applications would require a longer transmission line increasing losses and therefore adding to the noise figure of the system [32]. The previous examples suffered from poor levels of rejection that would often be considered unacceptable for a stand-alone notch filter design. Improvements were made to the in-

band gain reduction when resonators where incorporated in both arms of a wideband dipole resulting in a peak rejection of 29.4 dB [34].

An alternative solution to the unwanted signal rejection problem is to design a tunable, resonant antenna that only radiates at the frequencies of interest and naturally is an inefficient radiator elsewhere. One attempt was made by placing variable capacitors (varactors) at optimal locations along antennas such as loops, dipoles, and patches to vary the electrical length of the element therefore changing its self-resonant frequency. This approach was demonstrated using an optimized patch antenna that achieved a 2.67:1 tunable range [35]. Leveraging microfluidics has been shown to achieve a higher tunable range with stable performance across the band. A liquid metal monopole was fabricated that modulated the surface tension of a conductive liquid metal (EGaIN) to change the resonant frequency over a 2:1 range but suffered from long tuning times on the order of minutes, although the author admits to not optimizing the tuning time [36]. Using micropumps to move an insulating fluid and metal plate along a channel forming the shape of a monopole resulted in improved tuning times and radiation performance but was still limited to a 2:1 tuning range [37].

At a system level, a multi-antenna solution can aid in the rejection of unwanted interference. Consider a receiver which accepts two signals: the intended signal (f_1) with bandwidth (Δf_1) and unwanted signal (f_2) with bandwidth (Δf_2). If the front end of the radio is unable to discriminate between the two frequencies then there lies the possibility of f_1 to be hidden by f_2. A multi-antenna solution can be proposed that incorporates an adaptive cancelation scheme [22]. Adaptive cancellation entails a receive antenna, which accepts both f_1 and f_2, and a reference antenna, which ideally accepts f_2 at a higher power level than f_1. In the event that the intended signal is of known frequency and bandwidth and the unwanted signal is of unknown frequency

40

and bandwidth a reference antenna solution can be implemented that provides a wideband frequency response with a rejection band covering $f_1 \pm \Delta f_1/2$. This allows f_2 to be passed to the adaptive canceller and effectively removed from the receive antenna path.

This chapter presents the design of a symmetric spurline filter integrated directly into the radiating aperture of the periodic spiral antenna to introduce a rejection of up to 23 dB at the designed frequency. Derivation of the transmission equations for a symmetric spurline filter is presented and results are compared to full wave simulation. An equivalent transmission line model is developed to allow the antenna design to be decoupled from the filter design reducing computational resources. The location of the filter block along the length of the spiral arm is investigated and the frequency independent optimal location is discovered. A model is fabricated with the integrated notch filter in the optimal location and a lumped, high quality factor, capacitor is used to tune the resonance across the operational band of the spiral. The radiation characteristics are measured and correlation between the full wave equivalent transmission line model and measured results is presented.

4.2. Spurline Filter Design

The ability to design a spurline filter that fits into the width of a standard microstrip line makes this approach for integrating a rejection band very attractive. At the resonant frequency of a spurline filter the odd mode current distribution generated in the gap between the two conductors becomes dominant creating destructive interference in the through path of the signal line. Outside of the rejection band the magnitude of the even mode becomes proportionally larger and sustains the current distribution of a traditional transmission line.

Derivation of the set of equations that describe the frequency dependent operation of a spurline filter initially assumed that the even and odd mode phase velocity were equal. Equations

41

(4.1) – (4.8) show how to construct the transmission matrix for a spurline filter and equations (4.12) – (4.15) show the transformation from the ABCD matrix to the scattering matrix. While deriving equations (4.1) – (4.8) the spurline is treated as a section of coupled lines with a known impedance matrix. Boundary conditions, shown in equations (4.6) – (4.7), are then assigned at the input and output of the four-port impedance network to reduce it to a two-port impedance network which can then be expressed as a transmission matrix [38]. Leveraging the benefit of a transmission matrix allows it to be cascaded easily with other matrices to calculate the frequency dependent behavior of a more complex structure. Assuming the even and odd mode phase velocity are equal provides accurate results to determine the resonant frequency and rejection of the filter but miscalculates the quality factor of the filter. At the edge of the rejection band the even and odd mode phase velocity begin to differ and cause a variation in impedance. Incorporating separate variables for the separate phase velocities proved to correct this error [39].
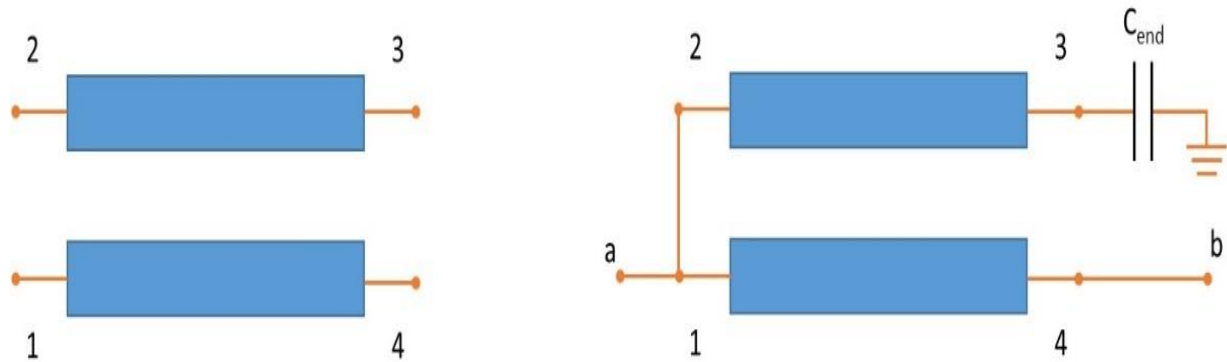
Figure 4.1. Transmission line model for coupled lines (left) and a spurline model showing the fringing capacitance at the termination of the stub (right).

$$\begin{bmatrix} V_1 \\ V_2 \\ V_3 \\ V_4 \end{bmatrix} = \begin{bmatrix} Z_{11} & Z_{12} & Z_{13} & Z_{14} \\ Z_{21} & Z_{22} & Z_{23} & Z_{24} \\ Z_{31} & Z_{32} & Z_{33} & Z_{34} \\ Z_{41} & Z_{42} & Z_{43} & Z_{44} \end{bmatrix} \begin{bmatrix} I_1 \\ I_2 \\ I_3 \\ I_4 \end{bmatrix} \tag{4.1}$$

42

$$Z_{11} = Z_{22} = Z_{33} = Z_{44} = -j \, {}^1\!/_2 \left(Z_{oe} \cot(\theta_e) + Z_{oo} \cot(\theta_o) \right) \tag{4.2}$$

$$Z_{12} = Z_{21} = Z_{34} = Z_{43} = -j \, {}^1\!/_2 \left(Z_{oe} \cot(\theta_e) - Z_{oo} \cot(\theta_o) \right) \tag{4.3}$$

$$Z_{13} = Z_{31} = Z_{24} = Z_{42} = -j \, {}^1\!/_2 \left(Z_{oe} \csc(\theta_e) - Z_{oo} \csc(\theta_e) \right) \tag{4.4}$$

$$Z_{14} = Z_{41} = Z_{23} = Z_{32} = -j \, {}^1\!/_2 \left(Z_{oe} \csc(\theta_e) + Z_{oo} \csc(\theta_e) \right) \tag{4.5}$$

$$V_a = V_1 = V_2, \ V_b = V_4, \ V_3 = \frac{-I_3}{J\omega C_{end}} \tag{4.6}$$

$$I_a = I_1 + I_2, \ I_b = -I_4 \tag{4.7}$$

$$\begin{bmatrix} A & B \\ C & D \end{bmatrix} = \begin{bmatrix} \cos(\theta) & jZ_{12}\sin(\theta) \\ j\sin(\theta)\left(\frac{1}{Z_1} + \frac{1}{Z_{12}}\right) & \cos(\theta) - \frac{Z_{12}}{Z_1}\sin(\theta)\tan(\theta) \end{bmatrix} \tag{4.8}$$

$$Z_1 = \frac{Z_o{}^{even}}{Z_o{}^{odd}} \left(\frac{Z_o{}^{even} + Z_o{}^{odd}}{2} \right) \tag{4.9}$$

$$Z_{12} = \frac{Z_o{}^{even} + Z_o{}^{odd}}{2} \tag{4.10}$$

$$Z_o = \sqrt{Z_o{}^{even} Z_o{}^{odd}} \tag{4.11}$$

43

$$S_{11} = \frac{A + B/Z_o - CZ_o - D}{A + B/Z_o + CZ_o + D} \qquad (4.12)$$

$$S_{12} = \frac{2(AD - BC)}{A + B/Z_o + CZ_o + D} \qquad (4.13)$$

$$S_{12} = \frac{2}{A + B/Z_o + CZ_o + D} \qquad (4.14)$$

$$S_{22} = \frac{-A + B/Z_o - CZ_o + D}{A + B/Z_o + CZ_o + D} \qquad (4.15)$$

The physical geometry of a spurline filter is shown in Figure 4.2 on the left and one embodiment of it integrated into a stripline structure is shown on the right. In this configuration W_{arm} is the width of the conductor determined by the antenna design, L_{stub} is the length of the spurline stub, G_{stub} is the width of the gap between the two conductors, H is the substrate thickness, and C_{tune} is the tuning capacitance that will later be used to adjust the resonant frequency. To validate the derived transmission matrix for a spurline filter a Matlab code was created and the full code is presented in the Appendix B. A full wave model was simulated in ANSYS Electronics Desktop 2016.2 consisting of a stripline with the embedded spurline filter surrounded by an ULTEM 1000 dielectric (ε_r = 3.15, tanδ = 0.0013) having a height (H) of 5.08 mm, L_{stub} = 25.4 mm, G_{stub} = 0.013 mm, conductor width = 5.08 mm, and ground width (W) equivalent to five times the width of W_{arm}. Maintaining the ground width (W) five times the width of the center conductor (W_{arm}) ensures that the impedance is not changed when the top and bottom ground conductors are electrically connected. While this ground plane width restriction creates a physical deviation from the orientation of the spiral arms it becomes a necessity as to not invalidate assumptions made in

44

the closed form solutions for stripline presented in [10]. Transmission equations were used to convert physical dimensions to an even and odd mode impedance of 130 Ω and 35 Ω, respectively. The results of the Matlab code and a full wave simulation are shown in Figure 4.3. There is a correlation in the rejection and resonant frequency but as expected the out of band performance is not well predicted by the set of equation which assume an equal even and odd mode phase velocity.
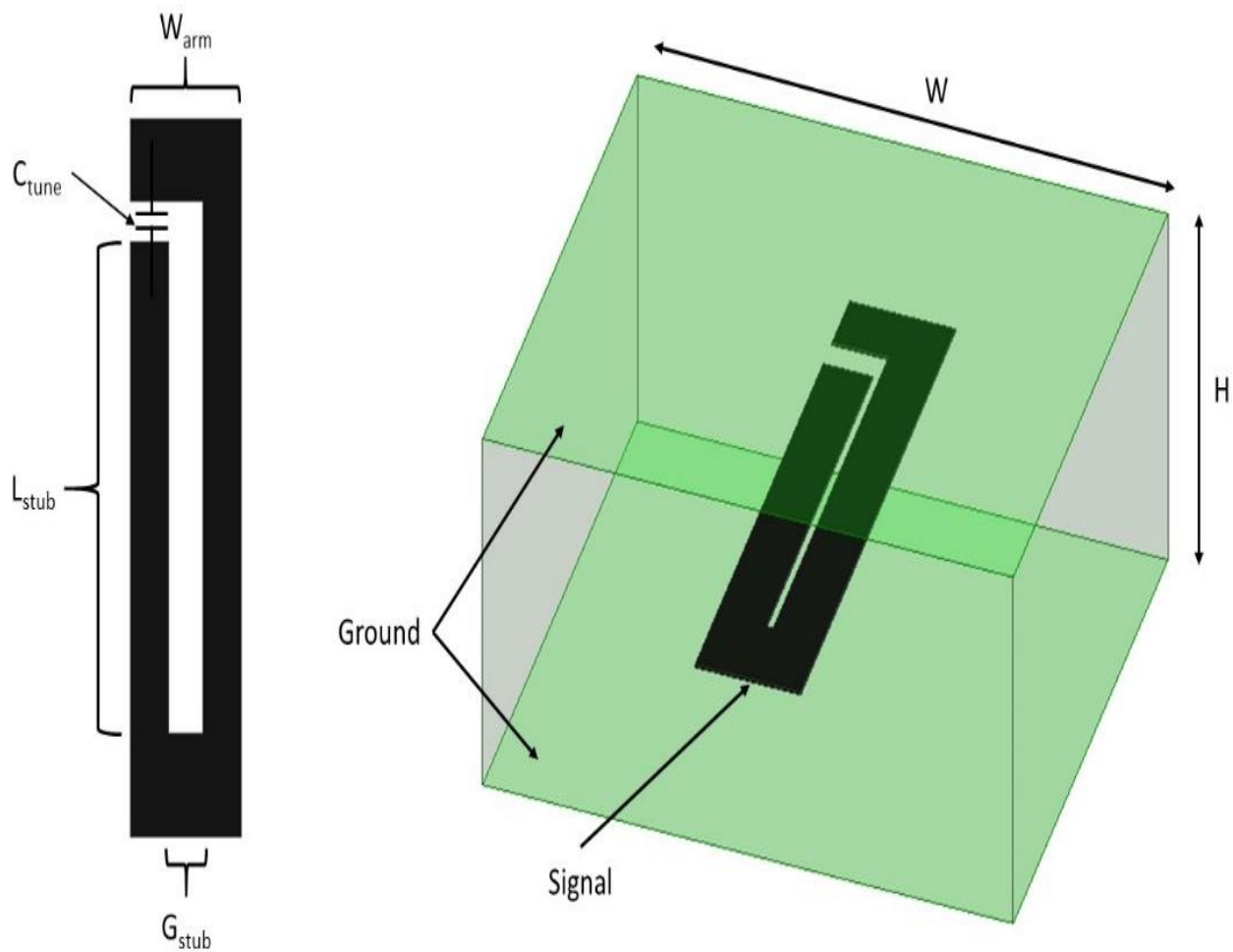

Figure 4.2. Full wave circuit model showing the spurline filter embedded into a stripline (right) and design parameters for the spurline filter (left).
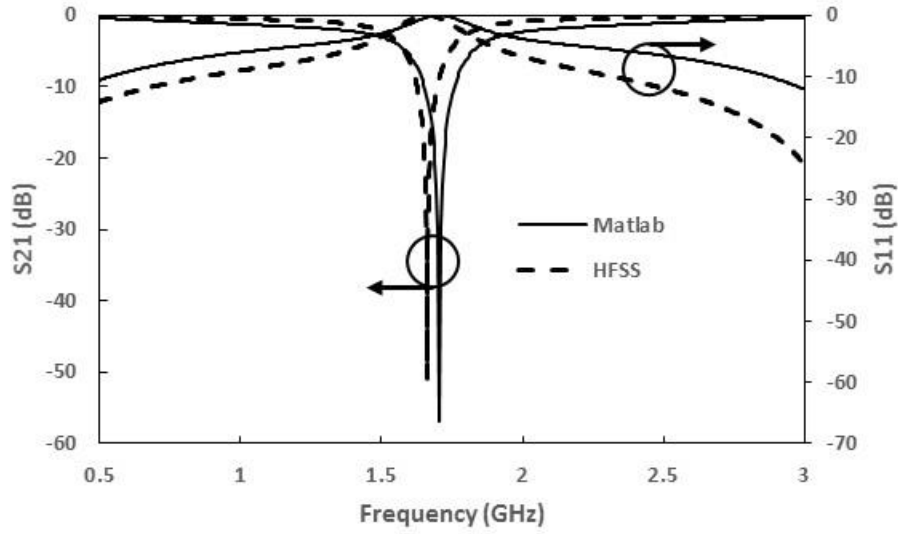
45

Figure 4.3. Comparison of full wave simulation and numerical analysis using ABCD matrix of coupled lines.

The design of a traditional spurline filter involves three design parameters: W_{arm} and G_{stub} combine to set the even and odd mode impedance and L_{stub} sets the length of the resonant stub which corresponds to $\lambda_g/4$. Figure 4.4 shows the insertion loss of the full wave circuit model described in Figure 4.2 while modulating the length of the stub (L_{stub}). For this study W_{arm} is held at 80 mils, G_{stub} is 5 mils, H is 200 mils, ε_r is 3.0, and no tuning capacitor (C_{tune}) is implemented. An increase in physical length correlates to a decrease in resonant frequency while maintaining the fractional bandwidth and symmetry of the filter about the center frequency. Once the stub length has been derived for the correct resonant frequency adjustments to the fractional bandwidth of the filter can be made by modifying the ratio of the even and odd mode impedance. To provide a bounded study for this correlation the overall width of the conductor (W_{arm}) was held constant and the width of the gap between the two conductors (G_{stub}) was varied. Results of this study are presented in Figure 4.5 showing a direct correlation between G_{stub} and fractional bandwidth where fractional bandwidth is defined here at the 10 dB rejection point. Since G_{stub} adjusts the ratio of

46

the even and odd mode impedances fractional bandwidth will not change with the length of the

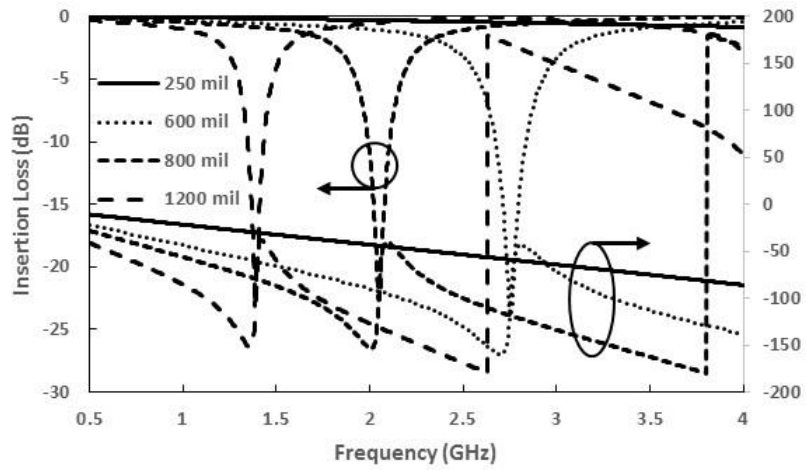stub (L_{stub}). Adjustments to G_{stub} resulted in less than 4.3% deviation in resonant frequency.

Figure 4.4. Insertion loss and phase response of the full wave circuit model with different stub lengths (L_{stub}).
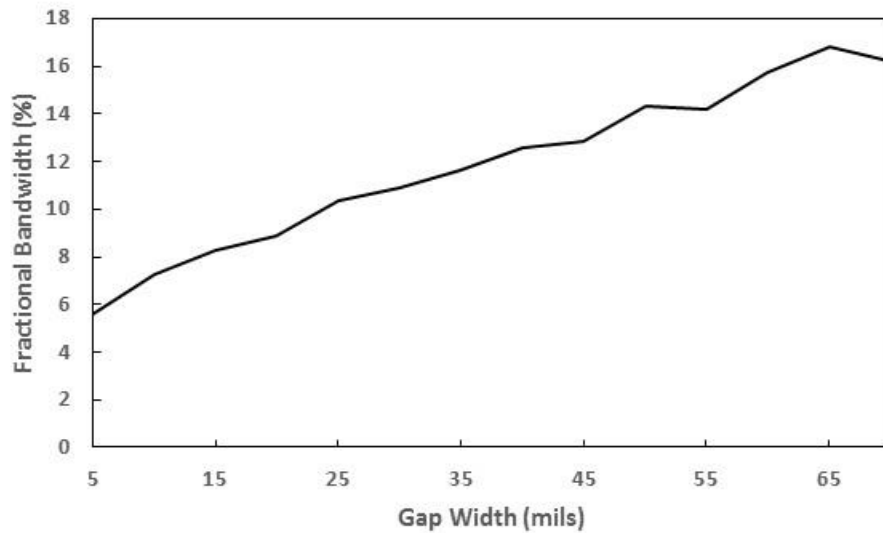

Figure 4.5. Fractional bandwidth of the full wave circuit model with different spurline gap values (G_{stub}).

Derivation of the transmission equations for a spurline filter presented in equations 4.1 – 4.15 define boundary conditions that reference the current at node I_3 to ground through the capacitive fringing fields at the end of the resonant stub. Therefore V_3 is defined as a function of a single variable in turn allowing the four-port impedance matrix presented in equation (4.1) to be reduced to a two-port scattering matrix. Figure 4.2 depicts a capacitor (C_{tune}) connecting the end of the stub to the adjacent signal line. This connection breaks down the previously established boundary conditions and therefore invalidates the derived scattering matrix. Defining new boundary conditions for the impedance matrix does not result in the ability to reduce the matrix to a two-port network so a new approach must be taken.

Full wave simulations in ANSYS Electronics Desktop 2016.2 demonstrate the tuning capability of placing a lumped capacitor at the end of the resonant stub. This simulation reduces L_{stub} to 6.4 mm while holding all other physical geometries the same as the prior study. Figure 4.6 depicts the frequency performance of the equivalent transmission line model with a rejection frequency of 2.6 GHz when C$_{tune}$ is 1 pF and 1.2 GHz when C$_{tune}$ is 6 pF while exhibiting a smooth phase transition outside of the rejection band. Figure 4.7 shows 1 W of incident power applied to the equivalent transmission line model and a calculated 45 V generated at the point of peak rejection with the voltage then decreasing exponentially away from the center frequency. Prior to the placement of this tuning capacitor power handling was limited solely to the thermal restrictions of the surrounding substrate. In regards to the relationship between generated voltage and incident power, Figure 4.8 displays the peak voltage across the terminals of a 2 pF capacitor and shows an exponential relationship described by equation (4.16) where *V* is the induced RF voltage and *x* is the incident power in logarithmic scale.
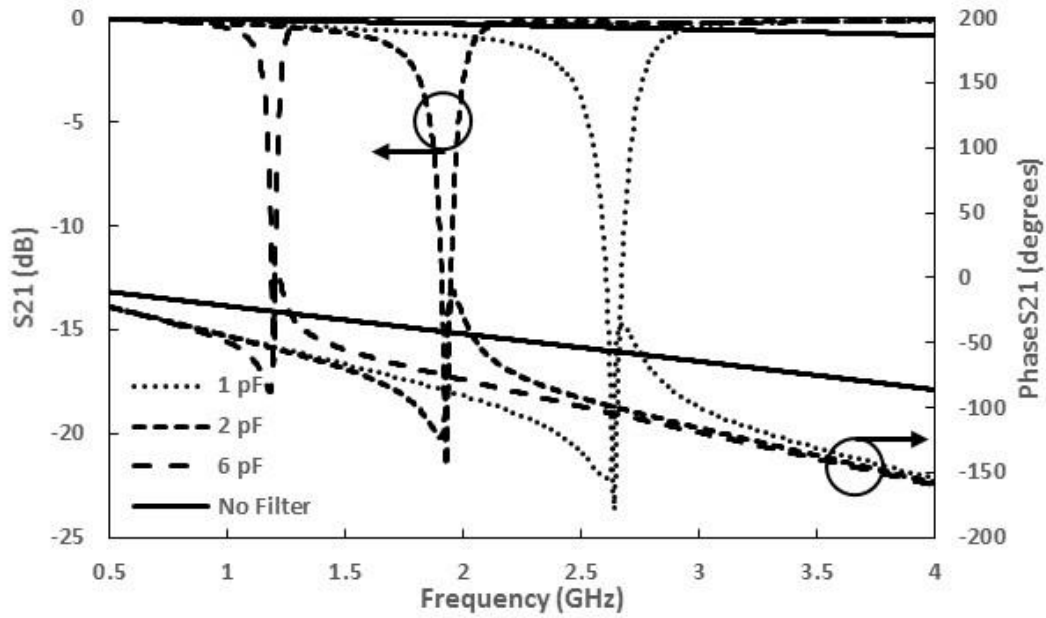
48

Figure 4.6. Insertion loss and phase response of the full wave circuit model with different tuning capacitors (C_{tune}).
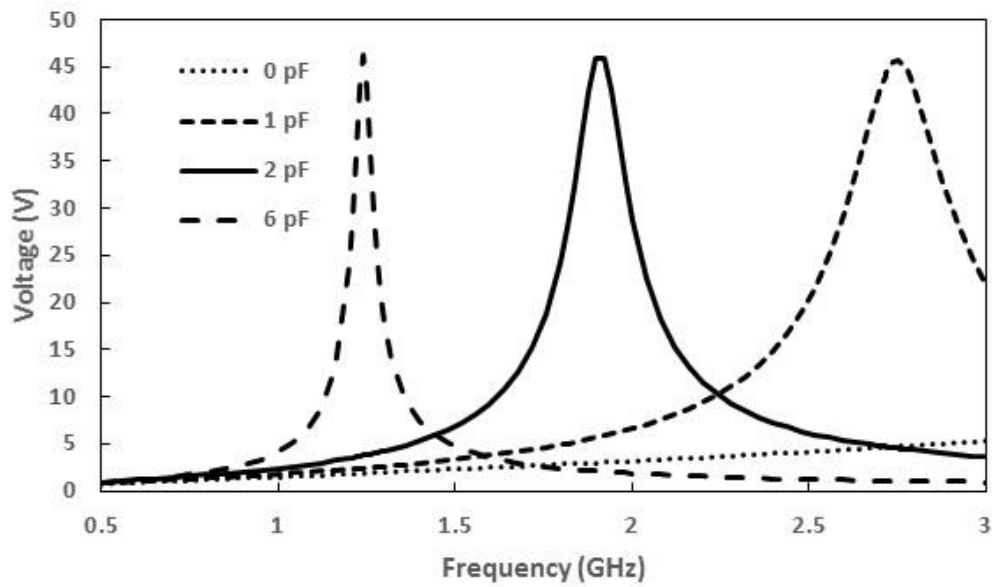

Figure 4.7. Full wave simulation results showing voltage generated at the resonant frequency of the symmetric spurline filter with different tuning capacitors (C_{tune}) and an incident power of 1 W.
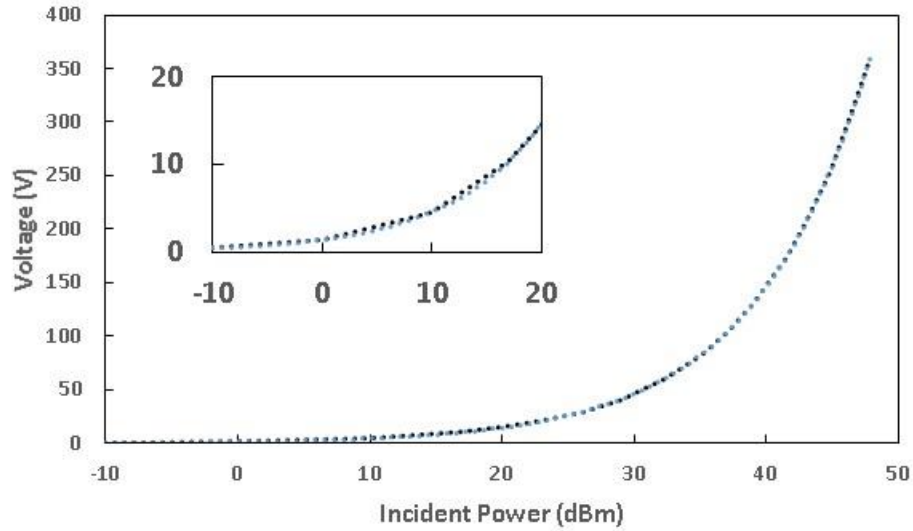
49

Figure 4.8. Full-wave simulation of peak voltage across the terminals of a 2 pF capacitor mounted at the end of the resonant stub.

$$V = 1.4643e^{0.1151x} \tag{4.16}$$

4.3. Filter Location Within a Spiral Antenna

In the proposed configuration, the filter is being integrated directly into the radiating aperture, therefore, the placement of the element along the length of the spiral arm is a critical design parameter. The aperture of a spiral antenna can be thought of as multiple concentric radiating loops combining to form the wideband frequency response. Each radiating loop is one wavelength in circumference lending to the low frequency region being defined by the outer portion of the spiral and the high frequency region being defined by the resolution of the feed in the center [40]. Given that the filter is replacing a portion of the spiral arms, it must be located such that radiation has yet to occur at the operational frequency of the filter and its out of band performance must not introduce loss or distort the phase. In general, for the filter to be effective over most of the bandwidth of the antenna it must be placed as close as possible to the feed. This

50

phenomenon was investigated further by placing a single stub spurline filter at distinct locations along the length of the spiral arm and tracking the level of rejection.

Three filters were designed, using the equivalent transmission line model shown in Figure 4.2, with different lengths to have resonant frequencies spanning the bandwidth of the antenna. These filters had lengths (L_{stub}) of 16.5, 25.4, and 40.6 mm to be self-resonant at 2.6, 1.7 and 1.2 GHz, respectively. For this study the length of the filter was changed as opposed to adding a lumped capacitor to the end of the stub to maintain the same notch rejection for each configuration and the amplitude of oscillation ($f(\theta)$ in equation (3.1)) for the spiral arms was set to zero to avoid meandering the filter. A depiction of the symmetric spurline filter embedded into a single arm of the spiral conductor is shown in Figure 4.9. A filter element was then placed in each arm of the 2-arm spiral at the same distance from the feed point. Identical filter elements were placed in each arm of the two-arm spiral at the same distance from the feed point and moved while calculating the achieved gain reduction at the center frequency of the filter. A visual of this arrangement can be seen in Figure 4.10. The shape of the antenna element matches that described in Section 3.2 and is shown in Figure 3.4.

Figure 4.9. Location and configuration of the symmetric spurline filter along the length of the spiral arm.
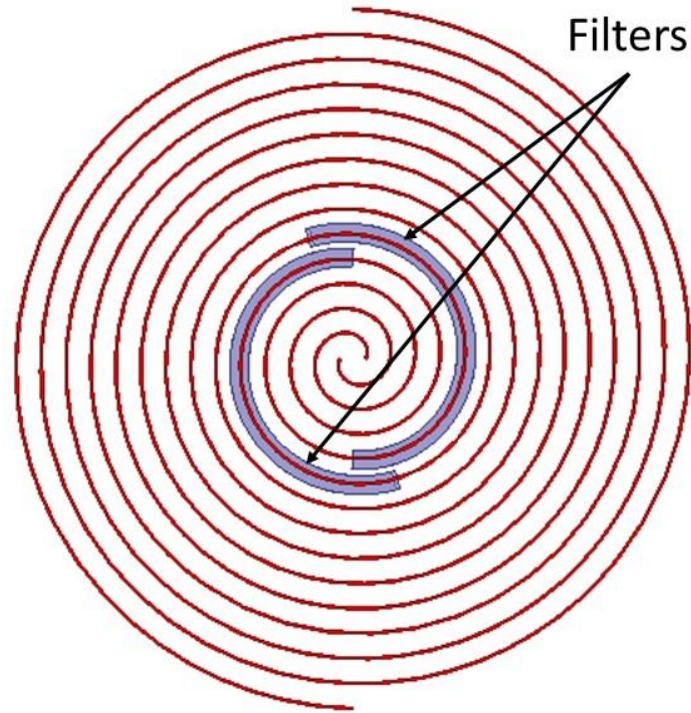
51

Figure 4.10. Top view of spiral antenna where the shaded regions depicts the placement of the filter in each arm. Specifically, this view shows the configuration where L_{stub} = 40.6 mm and the filters are placed 11 radians from the feed point.

ANSYS Electronics Desktop 2016.2 is used to compute the full-wave, frequency domain, electromagnetic solution. Simulation results comparing the angular distance from the antenna feed point with the achieved reduction in gain at the filters resonance are shown in Figure 4.11. For each filter, the highest level of rejection occurs when the filter is closest to the center and rejection degrades as the filter is moved along the length of the arm. As the resonant frequency of the notch filter decreases it is able to be moved further from the spiral center before its performance degrades, agreeing with the previous statement regarding the radiation rings within a spiral antenna. Tracking the 10 dB rejection point of each filter allows the beginning of the 2.6, 1.7, and 1.2 GHz filters to be placed 7.9, 11.0, and 20.4 radians from the feed point. This characteristic also shows the ability to cascade multiple filters into the radiating aperture and the optimal order

52

depending on their resonant frequency. When the filters are placed close to the feed point and are long enough to couple to the filter on the adjacent arm an oscillation in the rejection is observed. This is most apparent with the filter having a length of 40.6 mm when it was placed less than 15 radians from the feed point. Therefore, the optimal location of the rejection band filter becomes as close to the feed point as possible while avoiding overlap of the physical layout between adjacent arms.
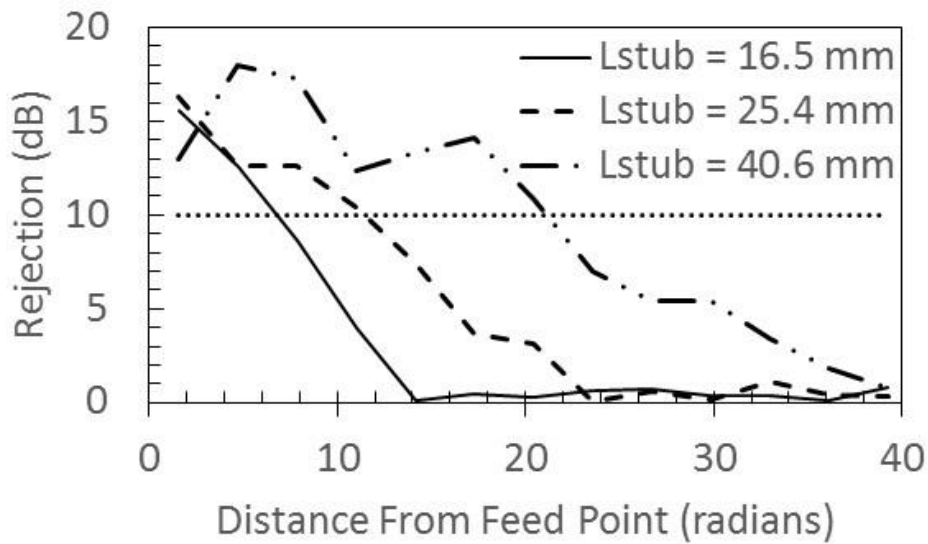

Figure 4.11. Rejection of single-stub spurline filter as a function of position along the arm of a spiral antenna.

4.4. Measured Results

The antenna is fabricated using the technique described in section 3.2 and is placed in the same sinuous cavity that was developed in [2]. The shape of the spiral arms is described in cylindrical coordinates by equation (4.17) and Table 4.1. Five models were built: one containing no filtering elements and four containing the symmetric spurline filter described by Figure 4.2 and

53

Table 4.2 placed π from the feed point of the spiral. The four models with the spurline notch filters were fitted with either 1 pF, 2 pF, 4 pF, or 6 pF high quality factor, lumped capacitors. Figure 4.12 shows the fabricated antenna model with the embedded notch filter.

$$\vec{r} = A\phi\hat{\phi} + (B\phi^c \sin(N\phi) - B\phi^c)\hat{z} \tag{4.17}$$

Table 4.1. Parameters for the cavity backed periodic spiral antenna.

A	0.8085 mm
B	46.526 nm
c	3
ϕ	$\pi/2 \leq \phi \leq 3.5\pi$

Table 4.2. Parameters for the symmetric spurline notch filter.

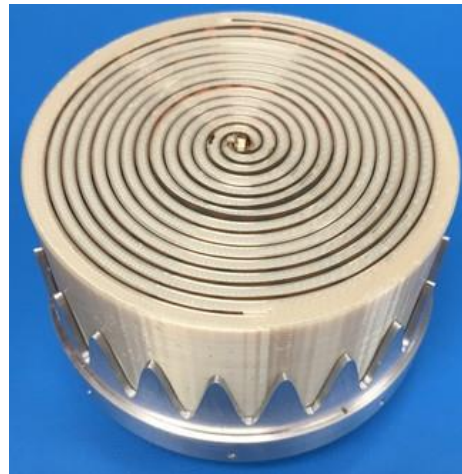| W_{arm}	2.032 mm
G_{stub}	0.127 mm
L_{stub}	6.096 mm

Figure 4.12. Fabricated periodic spiral antenna with embedded symmetric notch filter.

54

Radiation measurements were conducted in a MVG SG24C near-field chamber and numerical techniques were leveraged to transition the measurements to far-field data. Figure 4.13.a shows the filter's out of band effects on the broadside gain to be minimal while introducing 16 dB of rejection in-band. Figure 4.13.b through Figure 4.13.e show the predicted resonant frequency of the equivalent transmission line model compared to the fabricated antenna model with the corresponding filter configuration. Here the normalized broadside gain is plotted as a function of frequency and the insertion loss of a full wave simulation is conducted on the equivalent transmission line model as a means to quantify the rejection, quality factor, and resonant frequency deviation that occurs when the filter is embedded in the antenna. The resonant frequency of the 1 pF, 2 pF, 4 pF, and 6 pF loaded filters embedded into the spiral is 2.72, 1.88, 1.38, and 1.13 GHz, respectively. The peak deviation between the equivalent transmission line model and spiral antenna with the embedded filter was 4.38% for the resonant frequency and 20.28% for rejection. Additional gain rejection can be achieved by implementing cascaded filters of the same resonant frequency or designing a spurline filter which stacks multiple resonant stubs along the same length. Agreement amongst the equivalent transmission line model and the fabricated antenna shows the accuracy and usefulness of decoupling the filter design from the antenna design reducing computational resources. Figure 4.15 shows the calculated radiation efficiency across the band. The efficiency at the notch frequency is measured as 3.3%, 2.4%, 2.8%, and 3.0% for the filters loaded with 1 pF, 2 pF, 4 pF, and 6 pF, respectively. Orthogonal radiation pattern cuts are shown in Figure 4.16 for each notch frequency and the corresponding non-filtered model. No deviation in the radiation pattern is observed due to the integration of the filter element loaded with 2 pF, 4 pF and 6 pF capacitors and a null in the broadside is generated when loaded with the 1 pF capacitor. It is thought that this could be an effect of the cavity radiating due to energy traveling back down

the balun and is only noticeable now due to the higher level of achieved rejection. The broadside circular polarized phase across the operational bandwidth is shown in Figure 4.14 highlighting the phase deviation at the resonant frequency of the spurline filter fitted with a 2 pF lumped capacitor and a smooth phase transition in the remainder of the antennas operational bandwidth.
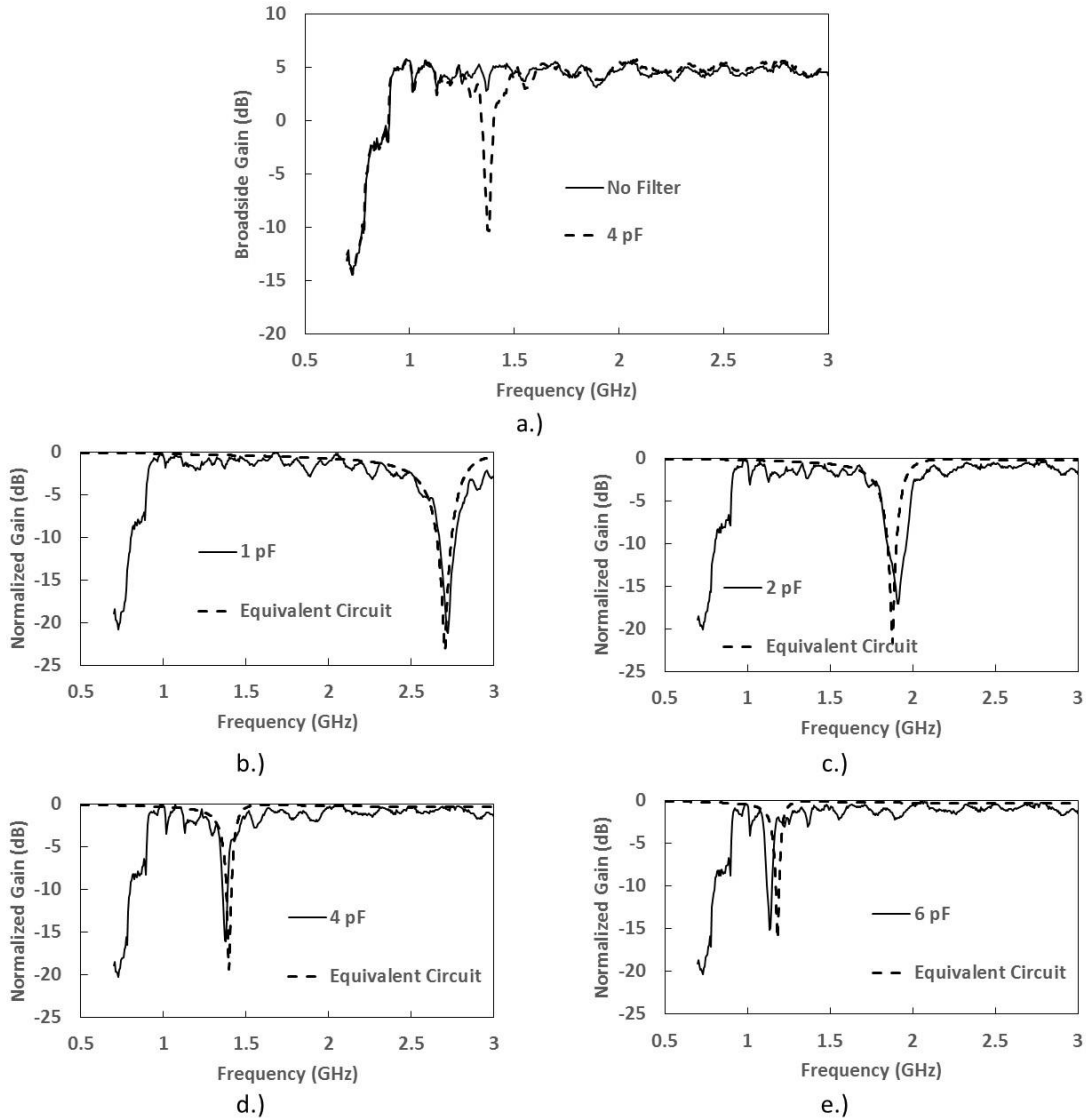

Figure 4.13. Comparison of the measured broadside realized gain for the cavity backed periodic spiral antenna with and without an embedded symmetric spurline filter (a). Comparison between insertion loss of equivalent transmission line model and measured normalized broadside gain for cavity backed periodic spiral antenna with embedded symmetric spurline filter loaded with 1 pF (b), 2 pF (c), 4 pF (d) and 6 pF (e).
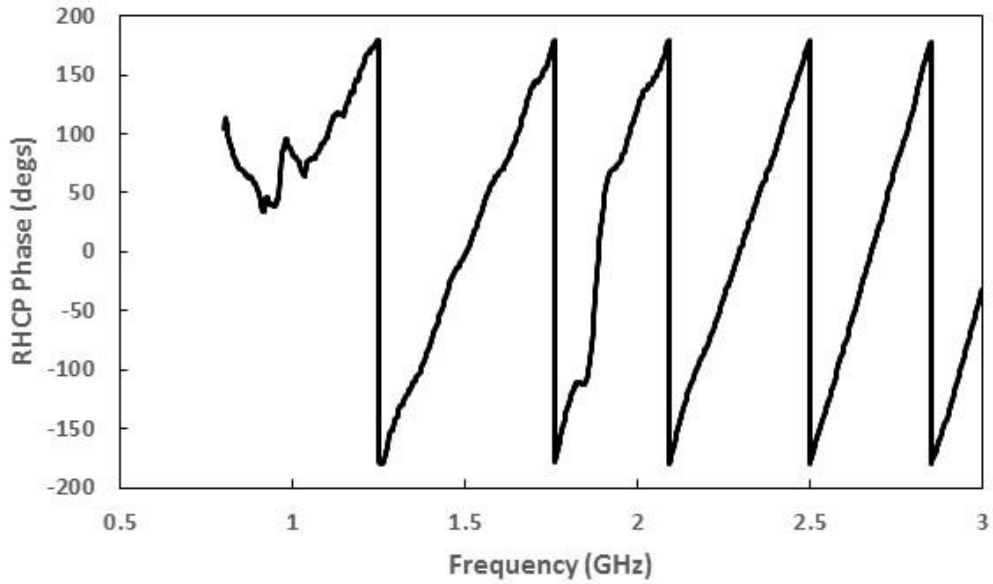
56

Figure 4.14. Broadside RHCP phase for the cavity backed periodic spiral antenna with an embedded spurline filter loaded with a 2 pF lumped capacitor showing a smooth transition outside the spurline filter resonant frequency (1.87 GHz).
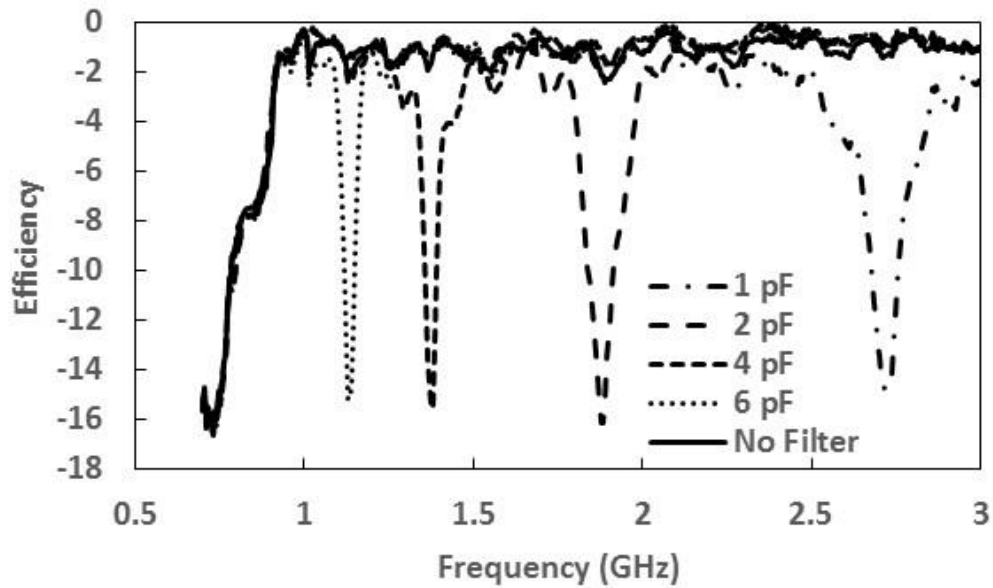

Figure 4.15. Efficiency of cavity back periodic spiral antenna without any filter elements as well as embedded with the symmetric spurline filter loaded with 1, 2, 4, and 6 pF.
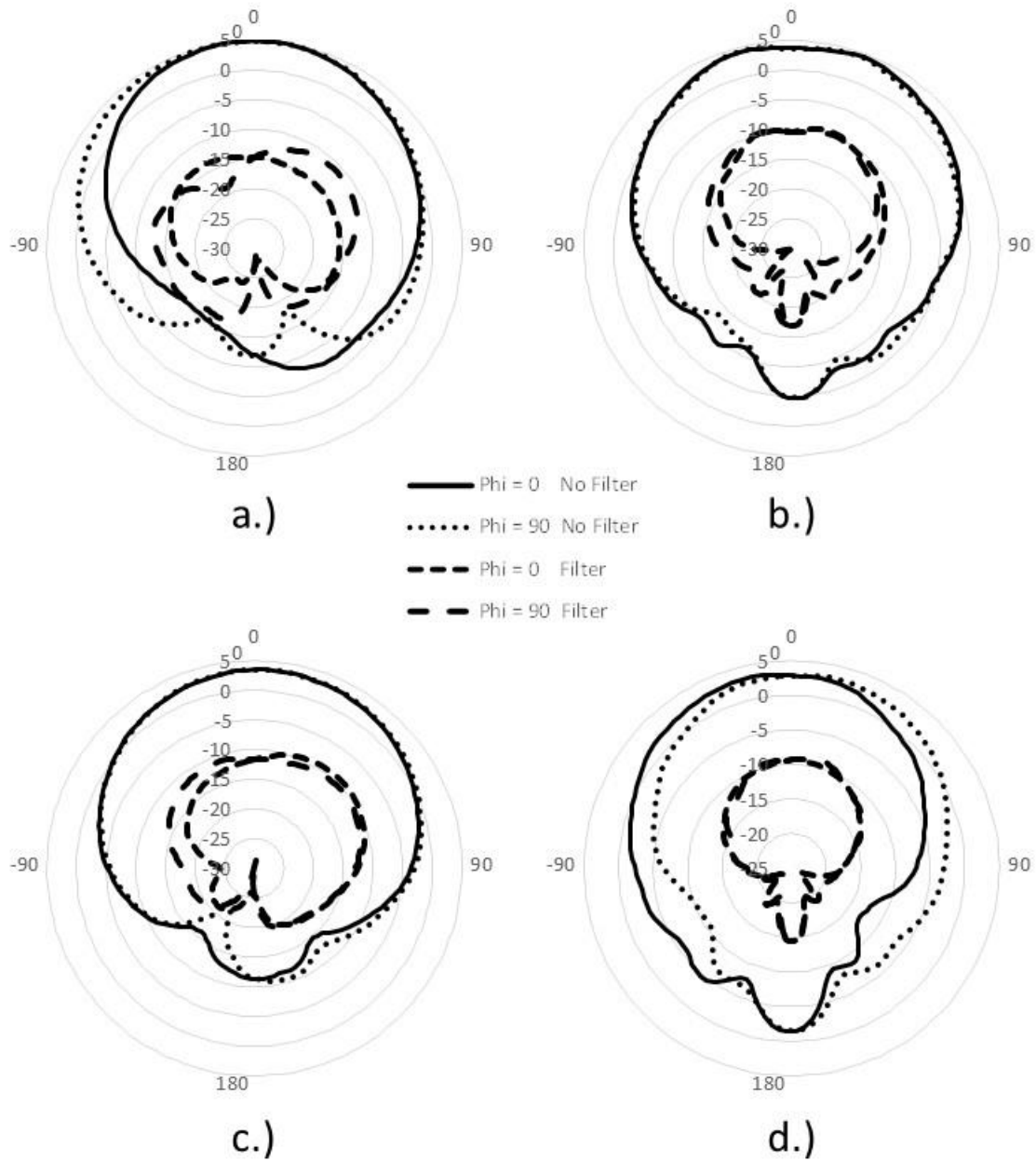
57

Figure 4.16. Orthogonal radiation pattern cuts of the cavity backed periodic spiral antenna comparing the model with no filter and the embedded symmetric spurline filter loaded with 1 pF (a), 2 pF (b), 4 pF (c), and 6 pF (d). Radiation patterns are plotted at the notch filters resonant frequency along with the corresponding unfiltered model.

58

CHAPTER 5: IMPROVED POWER HANDLING

5.1. Introduction

The law of conservation of energy dictates that energy cannot be created or destroyed but transferred from one state to another [27]. If we consider a transmission line structure, the inefficiencies due to dielectric and conductive losses represent loss mechanisms that transition electromagnetic energy into thermal generation. A study characterizing this phenomenon along the length of a microstrip line as a function of dielectric loss tangent and conductivity is presented in [4]. Chapter 3 proposes an equivalent transmission line model for the non-radiating portion of the periodic spiral antenna while Chapter 4 furthered the benefit of this model by demonstrating the ability to design a notch filter which is subsequently embedded into the radiating aperture. A lumped capacitor is demonstrated to lower the resonance of the spurline filter along with an increase in voltage across the terminals of the capacitor, as described in section 4.2. At the calculated voltage levels commercial available lumped capacitors become physically large in volume. The application described herein requires a low-profile design as to minimize interaction with adjacent arms while increasing the voltage handling capability. Voltage handling is increased by designed a tapered conductive sheet that is placed above the stub of the spurline filter. The two conductors are then separated from each other by a dielectric material creating a parallel plate capacitor with a dielectric breakdown voltage an order of magnitude above calculated values.

5.2. High Power Design Explanation

The dielectric breakdown of an insulator between two conductive plates of opposite polarities is a function of thickness. Equation (5.1) states that increasing the thickness of the insulator (*d*) by a factor of *x* requires an increase of the surface area (*A*) by the same factor in order to maintain capacitance using the same permittivity (ε) [10]. Therefore, in order to increase the voltage handling capability of a capacitive loaded symmetric spurline filter a tapered conductive wedge is designed and placed on top of the stub separated by an insulator to generate the required capacitance. Table 5.1 shows the configuration of the capacitive wedge where W^1_{wedge} is the width of edge 1, W^2_{wedge} is the width of edge 2, L_{wedge} is the linear length of the wedge, and *A* is the linear length of overlap between the capacitive wedge and the stub of the spurline filter separated by an insulator thickness of *d*. All other dimensional parameters are defined as they were in chapter 4. The transmission line model is equipped with the capacitive wedge described by Table 5.1 and the overlap (*A*) is swept to demonstrate the tuning capability of the capacitive wedge with a 10 µm thick Parylene insulator ($\varepsilon_r = 2.65, \tan \delta = 0.0006$) [41]. Figure 5.2 shows a tuning ratio of 2:1 with a rejection greater than 20 dB for all the explored overlap configurations.
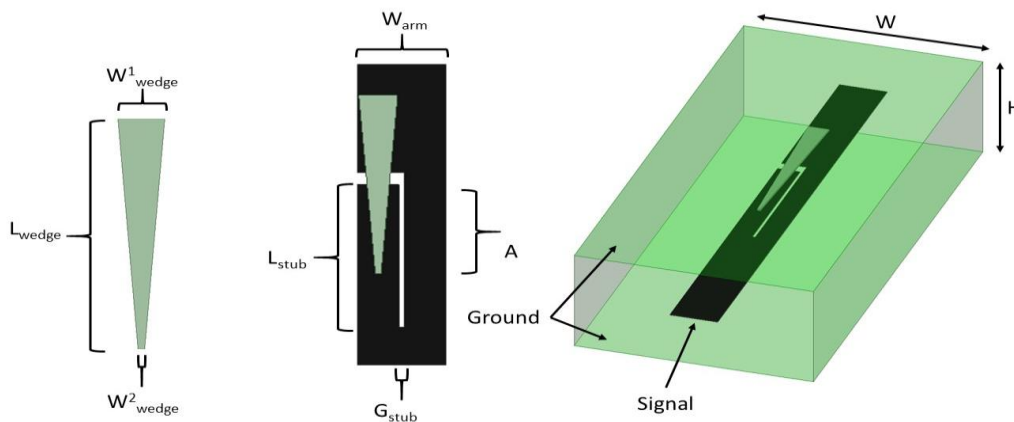

Figure 5.1. Full wave circuit model showing the spurline filter embedded into a stripline with integrated capacitive wedge (right), design parameters for the spurline filter (middle), and design parameters for the capacitive wedge (left).

60

$$C = \frac{\varepsilon A}{d} \qquad (5.1)$$

Table 5.1. Parameters for the symmetric spurline notch filter.

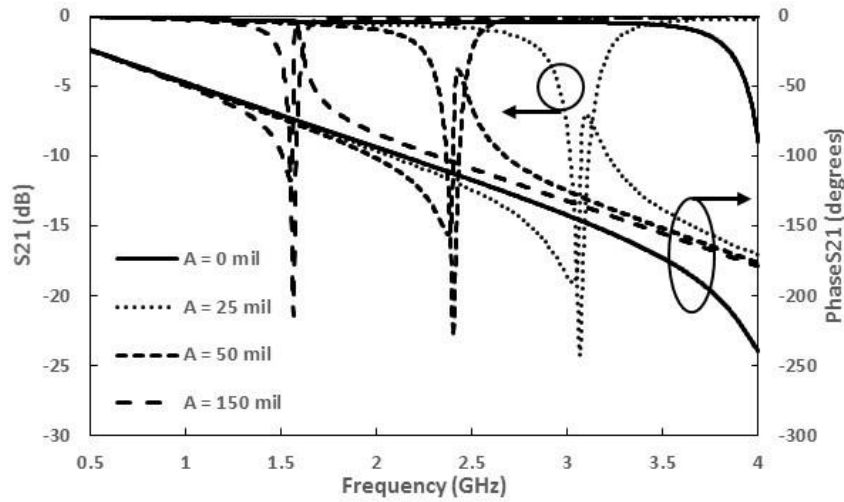|	
W^1_{wedge}	35 mil
W^2_{wedge}	5 mil
L_{wedge}	300 mil
d	10 µm

Figure 5.2. Insertion loss and phase response of the full wave circuit model with different values for the capacitive wedge overlap (A) and an insulator thickness of 10 um Parylene insulator.

Dielectric strength is a measurement that quantifies the amount of electric field that an insulator can withstand under ideal conditions prior to the material failing as an insulator [10]. The dielectric strength of Parylene N is 7,000 V/mil therefore the expected voltage handling of the aforementioned structure is 2,756 V [41]. The electric field within the Parylene that separates the capacitive wedge and the spurline stub is calculated using the full wave transmission line model. Understanding that this region contains a uniform electric field similar to that between the parallel plates of a capacitor allows the integral to be reduced as shown in equation (5.2). Verification of

61

the uniform electric field is shown in Figure 5.3 where the electric field vector is shown within the volume of the insulator and the complex magnitude of the electric field is plotted along a line the extends the length of the spurline wedge. Figure 5.4 calculates the simulated voltage potential across the insulator as a function of frequency for multiple values of overlap (A) with an incident power of 30 W. A familiar peak in induced voltage occurs when the rejection of the notch filter is maximum and decays away from this center frequency. An increase in the overlap (A), and therefore surface area, between the spurline stub and capacitive wedge results in a lower peak voltage as the magnitude of the electric field decreases due to the lower reactance. Figure 5.5 displays the peak generated voltage at the resonant frequency of the filter as a function of incident power for an overlap (A) of 25, 50, and 150 mils corresponding to a resonant frequency of 3.1, 2.4, and 1.6 GHz, respectively.
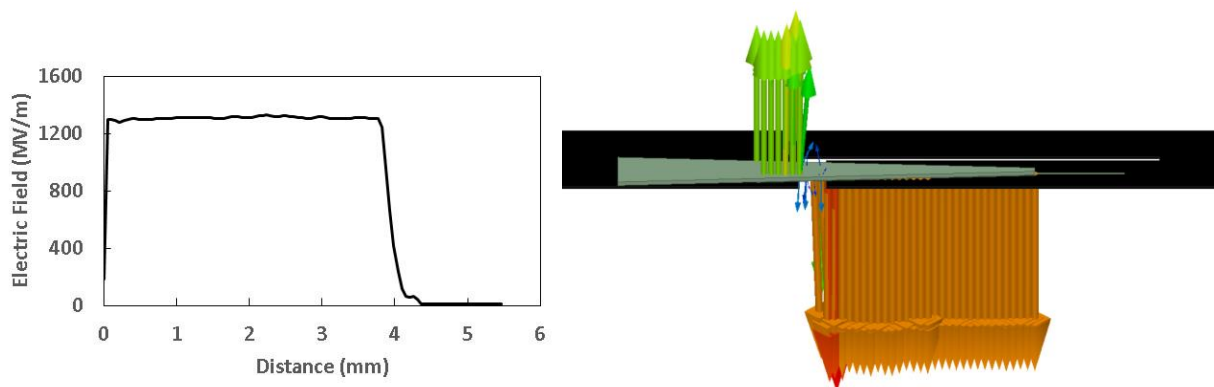
$$\Delta V = - \int E \cdot ds = |E|d \tag{5.2}$$

Figure 5.3. Simulated magnitude of the electric field present within the insulator as a function of distance (left) and the complex phase (right) at the frequency of peak rejection for an overlap (A) of 150 mils and an incident power of 30 W.
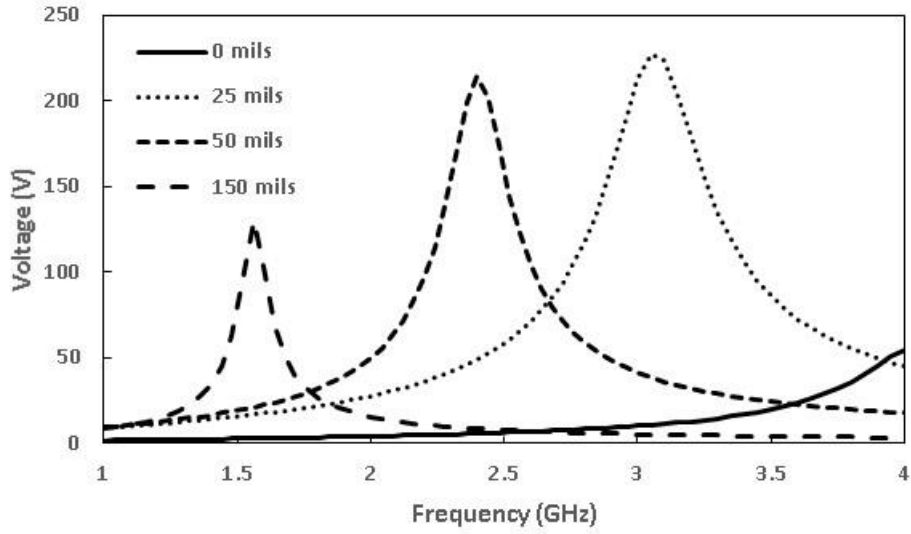
62

Figure 5.4. Full wave simulation results showing voltage generated between the capacitive wedge and the spurline stub for different values of overlap (*A*) with an incident power of 30 W.
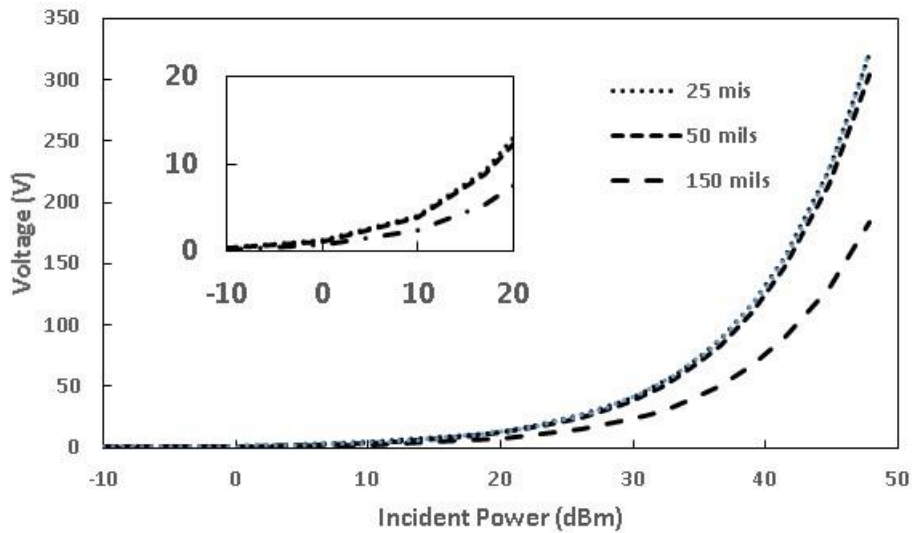

Figure 5.5. Full wave simulation showing peak voltage generated between the capacitive wedge and the spurline stub with an overlap (*A*) of 25 mils, 50 mils, and 150 mils corresponding to a resonant frequency of 3.1, 2.4, 1.6 GHz, respectively. Voltage is plotted at the resonant frequency of the filter.

63

5.3. High Power Measurements

The antenna presented in this section uses the same parameters, materials, and fabrication technique described in section 3.2 and utilized in section 4.4 for the model with lumped capacitors. Four models were built: one containing no filtering elements and three containing the symmetric spurline filter described by Figure 4.2 and Table 4.2 placed π from the feed point of the spiral. The shape of the capacitive wedge is described by Figure 5.1 with dimensional parameters detailed in Table 5.2. The wedge was fabricated using an etching process on a 1 mil thick LCP carrier substrate. The four models with the spurline notch filters were fitted with the capacitive wedge with an overlap (A) of either 75, 100, or 150 mils. Each configuration utilized a PET-based double-sided tape No.5601 manufactured by Nitto [42]. The tape consists of a PET (polyethylene terephthalate) carrier film deposited with an acrylic adhesive on both sides to a total thickness of 10 µm. Documentation shows a uniform shear and peel strength from temperatures between $10 - 80$ ℃. Figure 5.6 displays the measured difference in broadside gain between the model with no filter and the corresponding one with a 150 mil capacitive wedge overlap. At the resonant frequency of the notch filter the realized broadside gain is decreased by 12 dB while maintaining the same gain outside of the rejection band. An overlap of 75, 100, and 150 mil resulted in a resonant frequency 2.61, 2.25, 2.00 GHz, respectively, showing a discrepancy between the simulated values implementing a 10 µm insulator spacing. Adjustment of the transmission line model by increasing the insulator thickness to 18 µm resulted in the correct simulated resonant frequency which is shown by the dashed line in Figure 5.6. Figure 5.7 shows the simulated insertion loss and phase after the insulator thickness is updated to 18 µm displaying the reduced frequency tuning range. The measured efficiency shown in Figure 5.8 depicts the same logarithmic reduction as measured for the broadside gain. Orthogonal total gain radiation pattern cuts taken

64

for each filtered model at its respective peak rejection frequency as well the corresponding frequency of the unfiltered model is shown in Figure 5.9. The comparison between the two models show a uniform decrease in gain as a function of elevation.

Table 5.2. Updated parameters for the symmetric spurline notch filter.

W^1_{wedge}	35 mil
W^2_{wedge}	5 mil
L_{wedge}	300 mil
d	18 µm
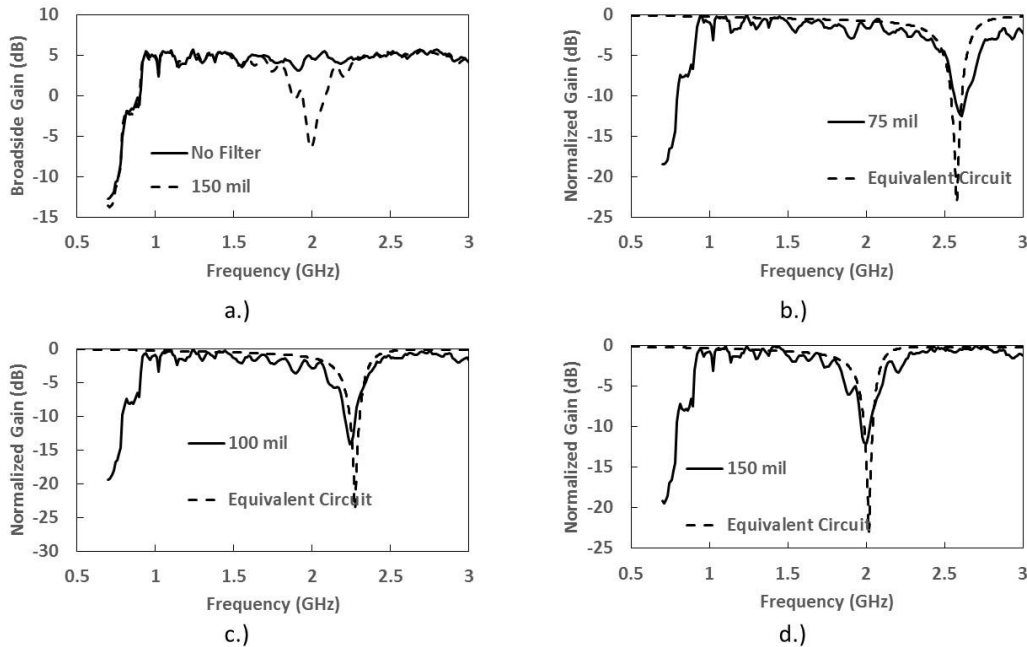
Figure 5.6. Comparison of the broadside realized gain for the cavity backed periodic spiral antenna with and without an embedded symmetric spurline filter loaded with the capacitive wedge with an overlap (A) of 150 mils (a). Comparison between insertion loss of equivalent transmission line model and normalized broadside gain for cavity backed periodic spiral antenna with embedded symmetric spurline filter loaded with the capacitive wedge with an overlap (A) of 75 mils (b), 100 mils (c), and 150 mils (d).

65
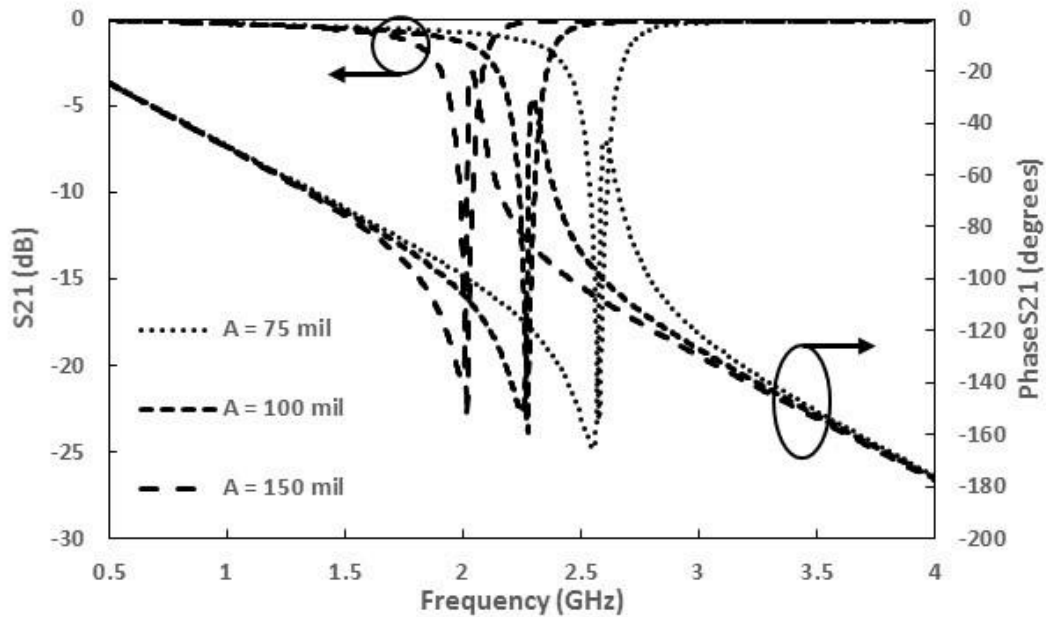
Figure 5.7. Insertion loss and phase response of the full wave circuit model with different values for the capacitive wedge overlap (A) and an insulator thickness of 18 um insulator.
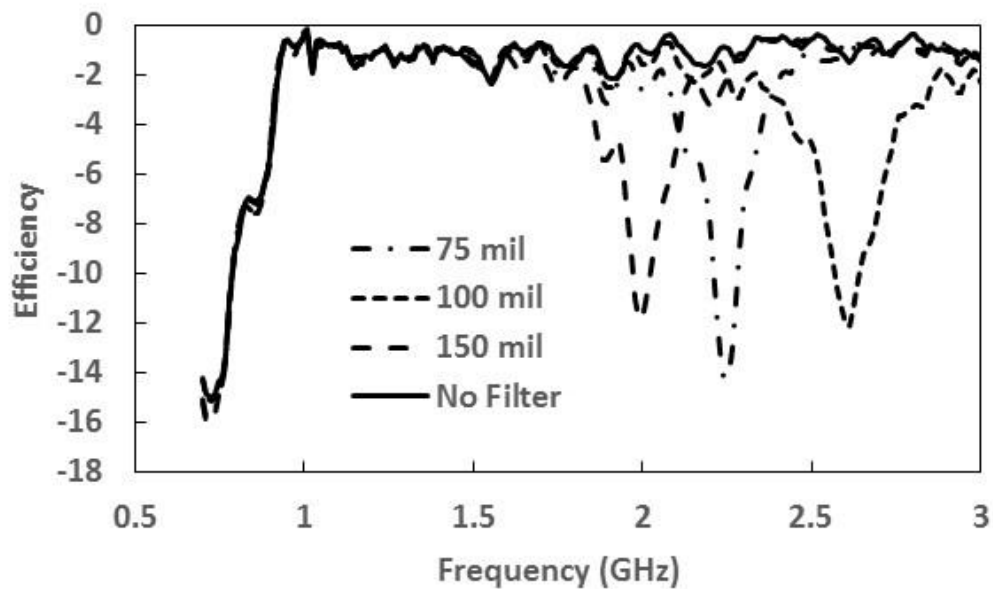

Figure 5.8. Efficiency of cavity back periodic spiral antenna without any filter elements as well as embedded with the symmetric spurline filter loaded the capacitive wedge with an overlap (A) of 75, 100, and 150 mils.
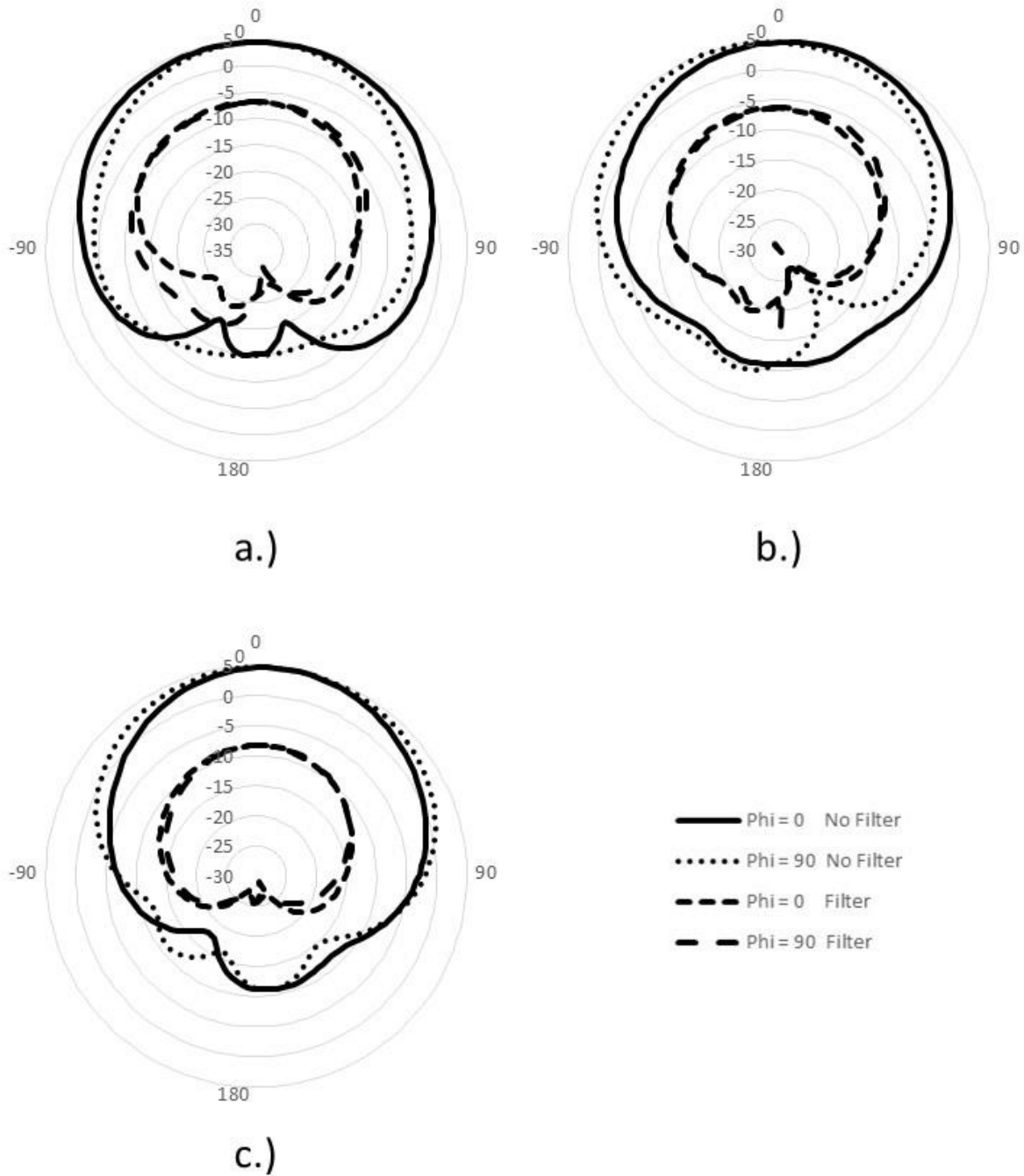
66

Figure 5.9. Orthogonal radiation pattern cuts of the cavity backed periodic spiral antenna comparing the model with no filter and the embedded symmetric spurline filter loaded with the capacitive wedge with an overlap (*A*) of 75 mils (a), 100 mils (b), and 150 mil (c). Total gain radiation patterns are plotted at the notch filters resonant frequency along with the corresponding unfiltered model.
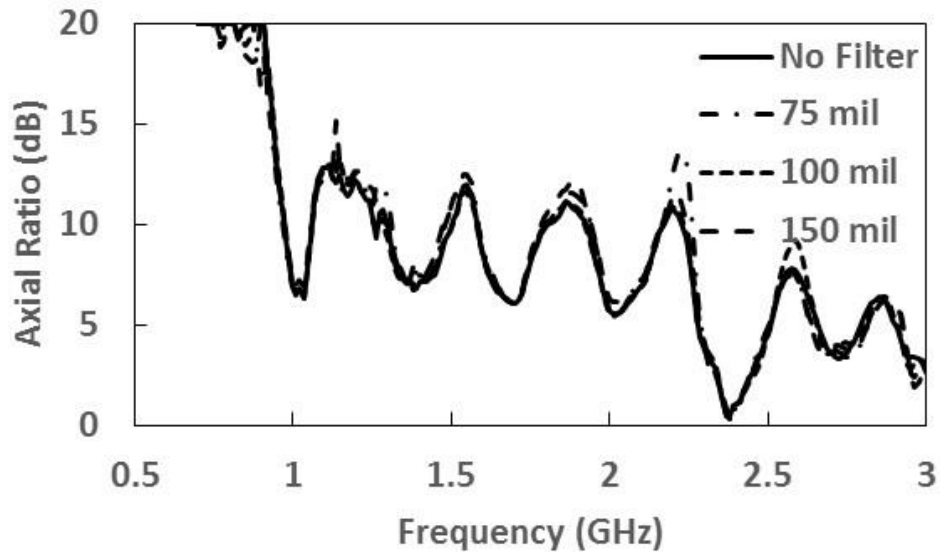
Figure 5.10. Axial ratio of cavity back periodic spiral antenna without any filter elements as well as embedded with the symmetric spurline filter loaded the capacitive wedge with an overlap (A) of 75, 100, and 150 mils.

5.4. Conclusion

Implementing a capacitive wedge into a spurline filter embedded into a periodic spiral antenna demonstrates the ability to tune the resonance of the rejection band filter while alleviating the power handling restriction imposed with a discrete capacitor. The low profile design minimizes interactions with the adjacent, out-of-phase, spiral arms as well as reduces the impact to the flexibility of the Polyimide substrate. The vapor deposited Parylene coating originally used as an insulator in the capacitive wedge proved to be difficult to adhere to the spurline filter without introducing addition thickness or non-uniformities. As an alternative, a 10 µm thick double-sided PET tape was used during the radiation measurements. This alternate solution showed a reduced tuning range while maintaining > 10 dB of gain rejection at all of the explored configurations. Simulations using the transmission line model show that an increase in insulator thick to 18 µm would explain the reduced tuning range.

68

CHAPTER 6: CONCLUSION

6.1. Summary

The prior development of the periodic spiral antenna revealed shortcomings in the assembly time, unit to unit repeatability, and accuracy of meandering the spiral arms. Addressing the fabrication approach for the periodic spiral antenna, the antenna substrate is modified to house a 5 mil thick, flexible, Polyimide substrate. This Polyimide substrate is wet etched to pattern the antenna elements with a resolution of microns while the arm spacing is maintained with the 3D printer resolution. These modifications result in the assembly time decreasing by a factor of 10.

The updated orientation of the antenna conductor increases the capacitive coupling between adjacent arms in the non-radiating portion of the antenna. Volume loss density plots show that this region, prior to the radiation band, now becomes the location of the largest concentration of loss, and therefore thermal generation. Power handling capability of the cavity backed periodic spiral antenna is quantified by thermal photographs taken with a FLIR camera which verify this heat distribution and reveal the frequency dependent nature of the radiation region. Successful power tests are conducted up to 60 watts at 1 and 2 GHz and up to 40 watts at 3 GHz.

Multi-purpose ultra-wideband radios in the presence of high-power, unwanted signals can be rendered ineffective if the interference is not properly addressed. Literature has identified methods for implementing rejection band filters into antennas, but has fallen short in its exploration beyond wideband dipole and monopole antennas. To address out of band interference concerns a symmetric spurline filter is implemented, for the first time, directly into the radiating aperture of a

69

spiral antenna. The design and optimization of the spurline filter is aided by the development of an equivalent transmission line model for the non-radiating portion of a spiral antenna, which allows the antenna and filter design to be executed separately. Implementing a lumped capacitor at the end of the spurline stub demonstrates its effectiveness to modulate the electrical length, and therefore resonance, of the filter. Measured results show up to 21 dB of rejection and the ability to tune the resonance over a 2.4:1 bandwidth.

The presented frequency dependent relationship between filter rejection and induced voltage reveals a need for a more robust solution when scaled for high power applications. This voltage restriction is addressed by implementing a capacitive wedge overlapping the spurline filter stub, separated by an insulating film, returning the power handling capability of the cavity backed periodic spiral antenna to its previously tested state. The design of the capacitive wedge included a 10 µm thick Parylene insulator which increases the voltage handling to 2,756 V. Difficulties in the physical implementation of the capacitive wedge resulted in replacing the intended 10 µm thick Parylene insulator with a double-sided, PET based adhesive tape demonstrating a reduced tuning ability.

6.2. Recommendations for Future Works

The integration of a symmetric spurline filter loaded with a capacitive wedge increases the voltage handling of the integrated filter. Chapter 5.3 held the capacitive wedge in place using a double-sided, PET based, adhesive tape introducing a method for static tuning of the resonant frequency of the filter. In applications where the interfering signal is of known, fixed frequency tuning times of the rejection band do not need to be fast. Alternatively, frequency hopping jamming sources may require a more adaptive tuning solution. One such approach to a more robust, dynamic

70

tuning solution to the placement of this capacitive wedge could include a non-conductive, mechanical piece that holds allows the wedge to be accurately slid along the spiral arm. Secondly, the spacing between the capacitive wedge and the spiral arm could be varied to modulate the achieved capacitance and therefore resonant frequency of the filter. Microfluidics could be incorporated by designing a channel that meanders between the two conductive sheets and allows for a low loss dielectric fluid to be passed through to change the effective permittivity of the medium. All of these solution include a controlled method to change the achieved capacitance while maintaining a higher dielectric breakdown than available with commercial lumped capacitors.

71

REFERENCES

[1]   O'Brien, Jonathan M., Thomas M. Weller, and John E. Grandfield. "Periodic spherical loop antenna." *Wireless and Microwave Technology Conference (WAMICON), 2015 IEEE 16th Annual*. IEEE, 2015.

[2]   O'Brien, Jonathan M., et al. "Miniaturization of a spiral antenna using periodic Z-plane meandering." *IEEE Transactions on Antennas and Propagation* 63.4 (2015): 1843-1848.

[3]   Balanis, Constantine A. "Antenna Theory: Analysis and Design." Hoboken, N.J: Wiley-Interscience, 2005.

[4]   O'Brien, Jonathan, "Medium Power, Compact Periodic Spiral Antenna" (2013). Graduate Theses and Dissertations.

[5]   Garg, Ramesh. Microstrip antenna design handbook. Artech house, 2001.

[6]   Lovato, Ricardo, Tianjiao Li, and Xun Gong. "Electrically tunable integrated patch antenna with planar filter." Wireless and Microwave Technology Conference (WAMICON), 2015 IEEE 16th Annual. IEEE, 2015.

[7]   Chen, Chun-Chyuan, and Chia-Chi Huang. "On the architecture and performance of a hybrid image rejection receiver." Selected Areas in Communications, IEEE Journal on 19.6 (2001): 1029-1040.

[8]   Katehi, P., and N. Alexopoulos. "On the effect of substrate thickness and permittivity on printed circuit dipole properties." Antennas and Propagation, IEEE Transactions on 31.1 (1983): 34-39.

[9]   James, J. R., A. J. Schuler, and R. F. Binham. "Reduction of antenna dimensions by dielectric loading." Electronics Letters 10.13 (1974): 263-265.

[10]   Pozar, David M. "Microwave Engineering." New York: Wiley, 1997. Print.

[11]   Bahl, I., Prakash Bhartia, and S. Stuchly. "Design of microstrip antennas covered with a dielectric layer." Antennas and Propagation, IEEE Transactions on 30.2 (1982): 314-318.

[12]   Nassar, Ibrahim T., and Weller, Thomas M. "An electrically small meandered line antenna with truncated ground plane." Radio and Wireless Symposium (RWS), 2011 IEEE. IEEE, 2011.

[13]   Lee, Ming, et al. "Distributed lumped loads and lossy transmission line model for wideband spiral antenna miniaturization and characterization." Antennas and Propagation, IEEE Transactions on 55.10 (2007): 2671-2678.

[14]   Wheeler, Harold A. "Fundamental limitations of small antennas." Proceedings of the IRE 35.12 (1947): 1479-1484.

[15]   Chu, Lan Jen. "Physical Limitations of Omni-Directional Antennas." Journal of applied physics 19.12 (1948): 1163-1175.

[16]   McLean, James S. "A re-examination of the fundamental limits on the radiation Q of electrically small antennas." Antennas and Propagation, IEEE Transactions on 44.5 (1996): 672.

[17]   Yaghjian, Arthur D., and Best, Steven R. "Impedance, bandwidth, and Q of antennas." Antennas and Propagation, IEEE Transactions on 53.4 (2005): 1298-1324.

[18]   Layne, Dennis. "Receiver Sensitivity and Equivalent Noise Bandwidth." *https://www.highfrequencyelectronics.com*. Harris Corporation. 2014. Web.

[19]   Lin, Chia-Ching, Peng Jin, and Richard W. Ziolkowski. "Single, dual and tri-band-notched ultrawideband (UWB) antennas using capacitively loaded loop (CLL) resonators." IEEE Transactions on Antennas and Propagation 60.1 (2012): 102-109.

[20]   Chung, Kyungho, Jaemoung Kim, and Jaehoon Choi. "Wideband microstrip-fed monopole antenna having frequency band-notch function." IEEE Microwave and Wireless Components Letters 15.11 (2005): 766-768.

[21]   Schantz, Hans Gregory, Glenn Wolenec, and Edward M. Myszka. "Frequency notched UWB antennas." Ultra Wideband Systems and Technologies, 2003 IEEE Conference on. IEEE, 2003.

[22]   Ghose, Rabindra N. *Interference Mitigation: Theory and Application*. New York: IEEE Press, 1996. Print.

[23]   Volakis, John L, Chi-Chih Chen, and K Fujimoto. "Small Antennas: Miniaturization Techniques & Applications." New York: McGraw-Hill, 2010. Print.

[24]   "Stratasys Production Series." Web. 1 Nov 2013. <http://www.stratasys.com/3dprinters/production-series>.

[25]   Guraliuc, Anda R., et al. "Numerical analysis of a wideband thick archimedean spiral antenna." Antennas and Wireless Propagation Letters, IEEE 11 (2012): 168-171.

[26]   Gilmore, David G. Spacecraft thermal control handbook. Aerospace Press, 2002.

[27]   McGrew, Ralph V, James A. Currie, Raymond A. Serway, and John W. Jewett. Instructor's Solutions Manual for Serway and Jewett's Physics for Scientists and Engineers, Sixth Edition, Volume One. Belmont, Calif: Thomson Brooks/Cole, 2004. Print.

[28]   Scialdone, John J., et al. "Atomic Oxygen and Space Environment Effects on Aerospace Materials Flown with EOIM-3 Experiment." (1996).

[29]   Kim, J., C. S. Cho, and J. W. Lee. "5.2 GHz notched ultra-wideband antenna using slot-type SRR." Electronics Letters 42.6 (2006): 315-316.

[30]   Chung, Kyungho, Jaemoung Kim, and Jaehoon Choi. "Wideband microstrip-fed monopole antenna having frequency band-notch function." IEEE Microwave and Wireless Components Letters 15.11 (2005): 766-768.

[31]   Lee, Wang-Sang, et al. "Wideband planar monopole antennas with dual band-notched characteristics." IEEE Transactions on Microwave Theory and Techniques 54.6 (2006): 2800-2806.

[32]   Lin, Chia-Ching, Peng Jin, and Richard W. Ziolkowski. "Single, dual and tri-band-notched ultrawideband (UWB) antennas using capacitively loaded loop (CLL) resonators." IEEE Transactions on Antennas and Propagation 60.1 (2012): 102-109.

[33]   Li, Tong, et al. "Compact UWB antenna with tunable band-notched characteristic based on microstrip open-loop resonator." IEEE Antennas and Wireless Propagation Letters 11 (2012): 1584-1587.

[34]   Schantz, Hans Gregory, Glenn Wolenec, and Edward M. Myszka. "Frequency notched UWB antennas." IEEE Proc., UWBST. 2003.

[35]   Sheta, Abdel-Fattah, and Samir F. Mahmoud. "A widely tunable compact patch antenna." IEEE Antennas and Wireless Propagation Letters 7 (2008): 40-42.

[36]   Wang, M., et al. "Pump-free feedback control of a frequency reconfigurable liquid metal monopole." 2015 IEEE International Symposium on Antennas and Propagation & USNC/URSI National Radio Science Meeting. IEEE, 2015.

[37]   Dey, Abhishek, and Gokhan Mumcu. "Microfluidically Controlled Frequency-Tunable Monopole Antenna for High-Power Applications." IEEE Antennas and Wireless Propagation Letters 15 (2016): 226-229.

[38]   Nguyen, C., and C. Hsieh. "Millimeter wave printed circuit spurline filters." Microwave Symposium Digest, 1983 IEEE MTT-S International. IEEE, 1983.

[39]   Bates, R. N. "Design of microstrip spur-line band-stop filters." IEE Journal on Microwaves, Optics and Acoustics 1.6 (1977): 209-214.

74

[40]   Wheeler, M. "On the radiation from several regions in spiral antennas." Antennas and
        Propagation, IRE Transactions on 9.1 (1961): 100-102.

[41]   http://www.parylene.com/pdfs/PTC-Parylene_Properties_Chart.pdf

[42]   http://form.nitto.com/us/en/products/group/double/037/index.jsp

APPENDIX A: TAPERED BALUN DESIGN AND SIMULATED RESULTS
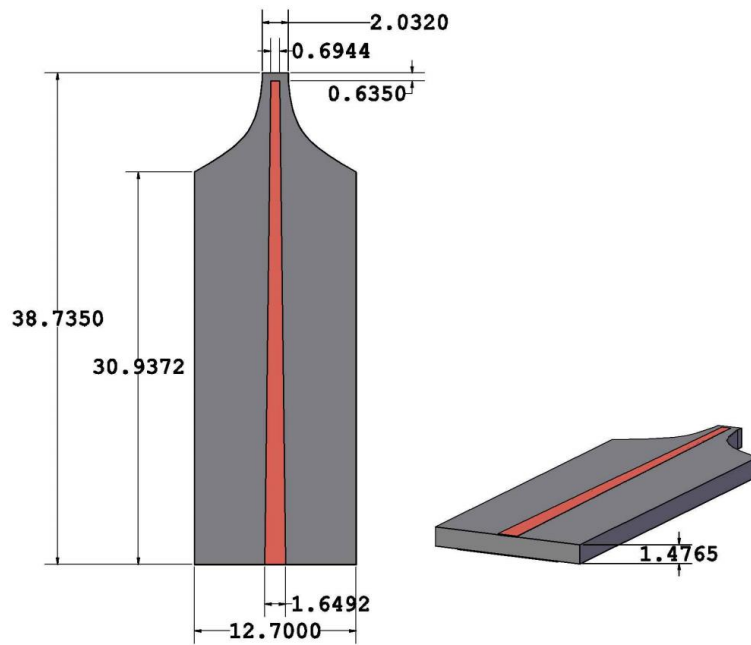
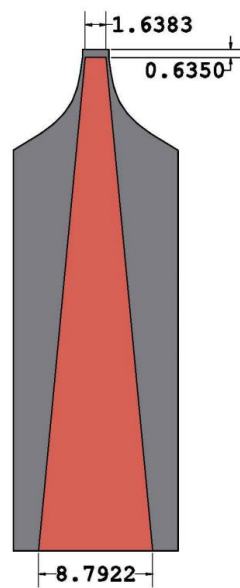Figure A.1. Top and profile view of balun showing dimensions in mm
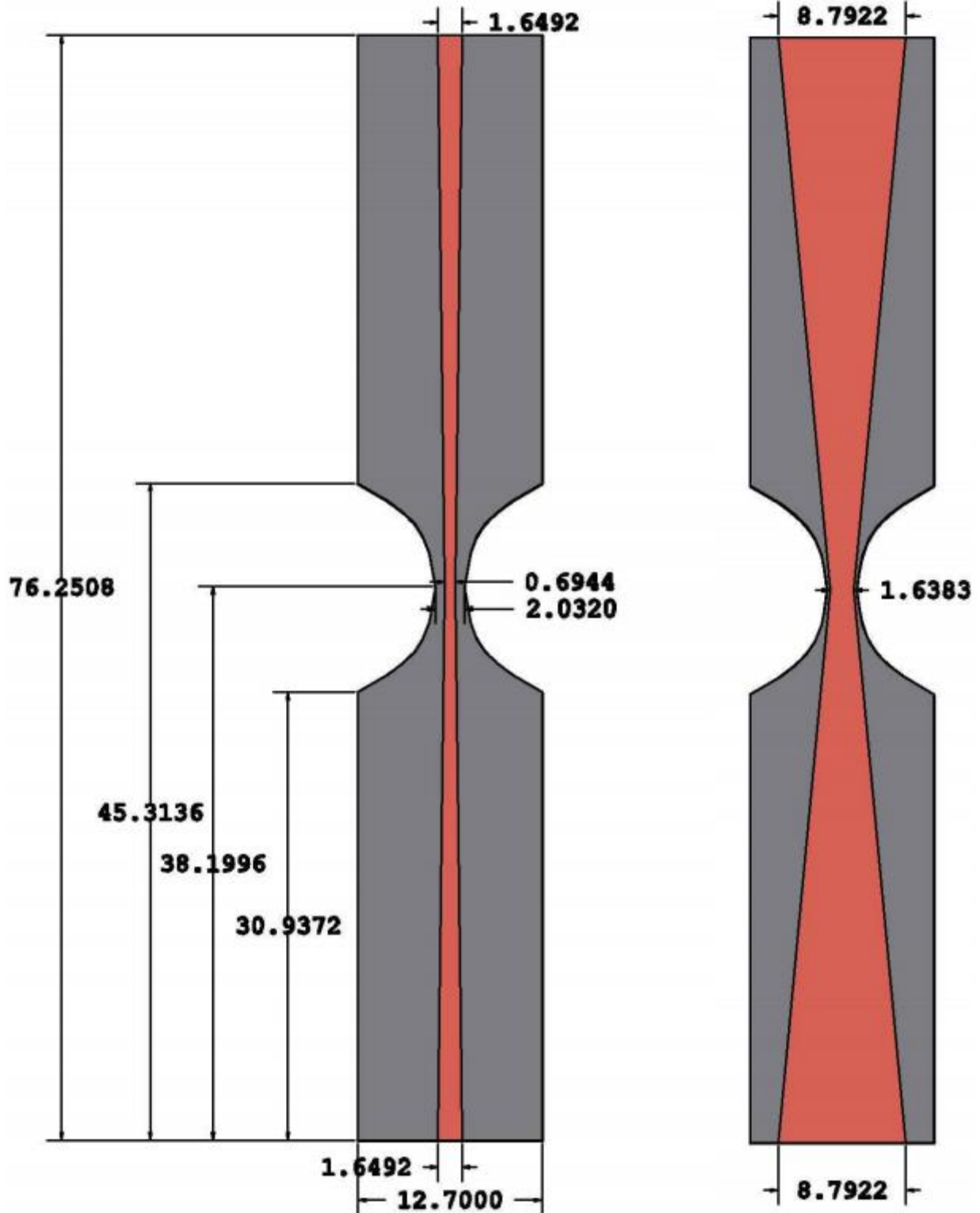

Figure A.2. Bottom view of balun showing dimensions in mm

Figure A.3. Top and bottom view of back to back balun used for measurement and simulation verification showing dimensions in mm
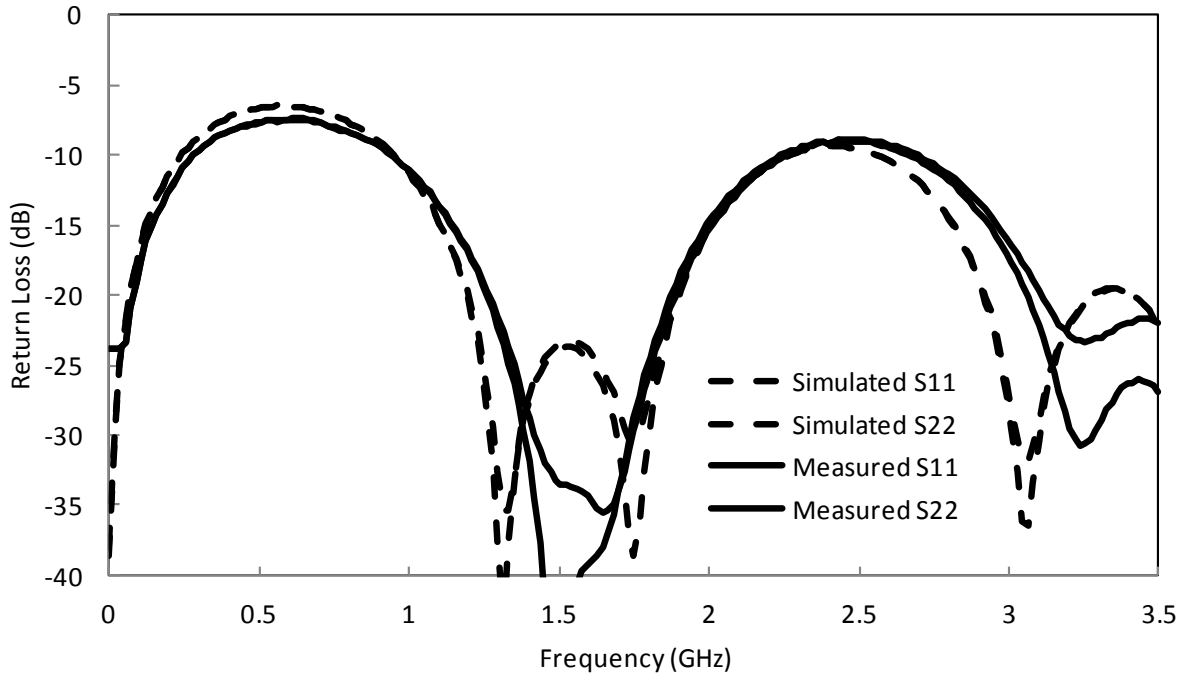
Figure A.4. Measured and simulated return loss of back-to-back balun used for performance verification
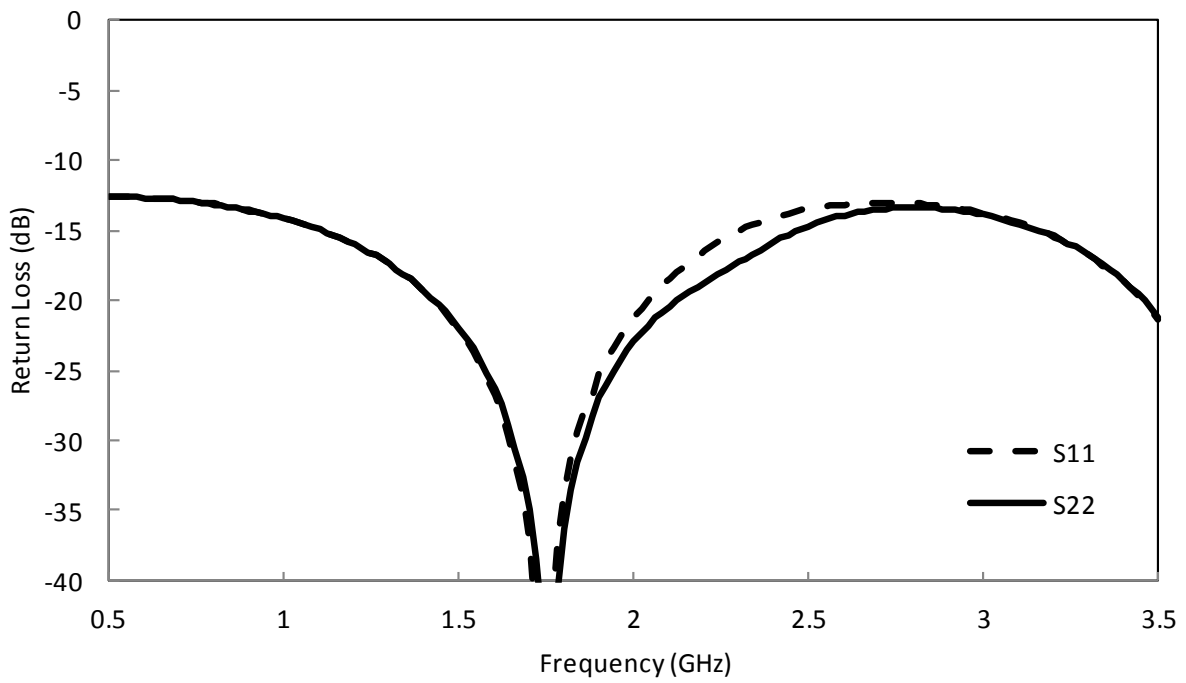
Figure A.5. Simulated return loss of single balun used to feed both PSA antenna models

78

APPENDIX B: MATLAB CODE FOR SYMMETRIC SPURLINE

```matlab
%% Spurline Filter Analysis

close all; clear all; format compact; clc; format long;

%% Constants
c = 3e8;
l = 1.4*0.0254;
Er = 4.4;
f_start = 0.5e9;
f_end = 1.5e9;
f_step = 0.001e9;


C_end = 4e-14;


Zoe = 70;
Zoo = 30;
Zo = sqrt(Zoo*Zoe)
f = f_start;
x = 1;


Z1 = Zoe/Zoo*(Zoo + Zoe/2);
Z12 = Zoo + Zoe/2;
while f <= f_end
    w = 2.*pi.*f;
    lambda = c./(f*sqrt(Er));
    beta = 2.*pi./lambda;
    theta = beta.*l;                % Assume even and odd mode have same phase
velocity


    %% Define ABCD matrix

    A = cos(theta);
    B = 1i*Z12*sin(theta);
    C = 1i*sin(theta)*(1/Z1 + 1/Z12);
    D = cos(theta) - Z12/Z1*sin(theta)*tan(theta);

    ABCD = [A B; C D];

    s_matrix(:,:,x) = abcd2s(ABCD,50);
    f = f + f_step;
    x = x + 1;

end
```
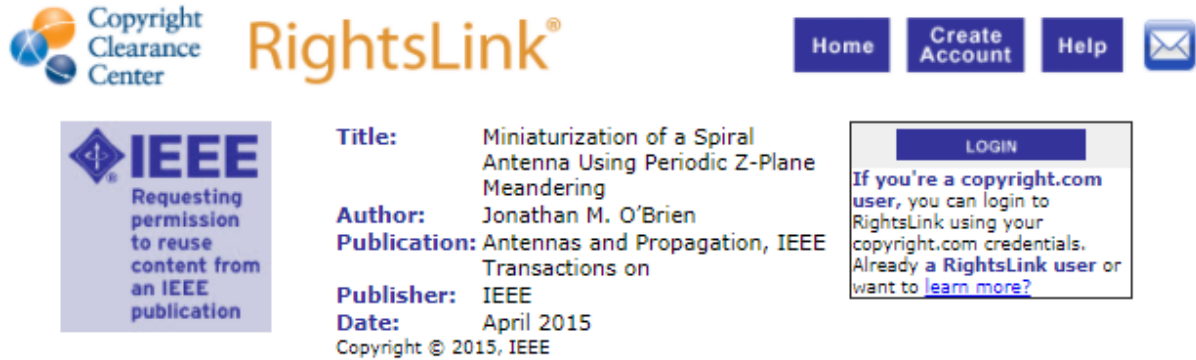
```
figure
freq_sweep = f_start:f_step:f_end;
S11 = abs(s_matrix(1,1,:));
plot(freq_sweep,20*log10(S11(:)))
hold on
S21 = abs(s_matrix(2,1,:));
plot(freq_sweep,20*log10(S21(:)),'r')
```

APPENDIX C: COPYRIGHT PERMISSIONS

Below is permission for the use of the images in figures 3.1

81

ABOUT THE AUTHOR

Jonathan O'Brien received his B.S. degree in Electrical Engineering in 2012 from the University of South Florida. Towards the end of his bachelor's degree, he worked for a small engineering company tasked with designing self-test systems for the Orion Shuttle project. His graduate studies were first sponsored by nScrypt and Sciperio. During this time, he researched and characterized additive manufactured materials for RF applications. He was then the recipient of a Draper Labs fellowship where he concentrated on advanced antenna design. Jonathan O'Brien now works in the RF & Comm Systems group at Draper.